Title

Understanding the Crosstalk Between Lipid Metabolism in Innate Immune Cells and Host Defense against Bacterial Toxins

Author

Lee, Min

Publication Date

2024

Peer reviewed|Thesis/dissertation

UNIVERSITY OF CALIFORNIA

Los Angeles

Understanding the Crosstalk Between Lipid Metabolism in Innate Immune Cells and Host Defense against Bacterial Toxins

A dissertation submitted in partial satisfaction of the

requirements for the degree Doctor of Philosophy

in Molecular and Medical Pharmacology

by

Min Sub Lee

2024

ABSTRACT OF THE DISSERTATION

Understanding the Crosstalk Between Lipid Metabolism in Innate Immune Cells and Host Defense against Bacterial Toxins

by

Min Sub Lee

Doctor of Philosophy in Molecular and Medical Pharmacology

University of California, Los Angeles, 2024

Professor Steven J. Bensinger, Chair

Necrotizing fasciitis (NF) is a severe bacterial infection characterized by extensive tissue destruction of skin and underlying fascia. The development of NF can be rapid and requires immediate hospitalization. Treatment requires aggressive, surgical debridement of involved tissues, resection of surrounding healthy tissues, accompanied by systemic antibiotics. Even with these extreme therapeutic measures, mortality can reach upwards of 30% for patients. Thus, a better understanding of host factors that predispose individuals to the rapid and extensive tissue damage observed in necrotizing fasciitis and other necrotizing soft tissue infections remains imperative.

Metabolic dysfunctions such as diabetes and obesity have been reported as risk factors for NF. We show that Western diet-feeding of mice increases the magnitude of tissue destruction from necrotizing Group A *Streptococcus* (GAS; *S. pyogenes*) skin infection. The increased tissue destruction is not observed in mice a fed a high-fat diet, indicating that the effect was specific to cholesterol-enriched Western diet rather than a consequence of obesity *per se*. Remarkably, the increased tissue destruction observed in Western-diet fed mice is dependent on the expression of the pore-forming toxin Streptolysin-O (SLO), a member of the cholesterol-dependent cytolysins (CDCs).

Because SLO is known to target cholesterol in the host plasma membrane, we reasoned that cholesterol metabolism could be a targetable signaling axis to combat SLO-induced tissue destruction. Liver X receptor (LXR) is a set of nuclear receptors that transactivate a broad number of genes implicated in lipid homeostasis, such as cholesterol efflux and inhibition of cholesterol import. We show that treatment of GW3965, a potent LXR agonist, on mice skin reduced SLO-induced tissue damage, both prophylactically and as late as 6h post-SLO challenge.

Our shotgun lipidomics reveal that LXR activation leads to decreased abundance of lysophosphatidylcholine (LPC). Mechanistically, we discover that modulating host LPC homeostasis influences the magnitude of tissue destruction to SLO toxin alone and in GAS infection by modulating the accessibility of cholesterol targeted by SLO. The recognition that diet and the lipid metabolic state of individuals regulates the degree of tissue destruction in GAS infection advances our understanding of the pathogenesis of these challenging infections.

The dissertation of Min Sub Lee is approved.

Elizabeth J. Aguiar Vallim

Jeffery F. Miller

Philip O. Scumpia

Ting-Ting Wu

Steven J. Bensinger, Committee Chair

University of California, Los Angeles

2024

Dedication

To my mother, Nam Seon Lee,

My girlfriend, Hannah Kim

And my friends and colleagues

Table of Contents

Abstract of the Dissertation……ii

Dedication……v

Table of Contents……...vi

Acknowledgements……...vii

Vita……x

Chapter 1: Necrotizing Fasciitis, Group A Strep, and Cholesterol-Dependent Cytolysins…….1

Methods……..12

Figure Legend……...14

Figure 1. ……15

Chapter 2: Cholesterol Homeostasis and CDC activity……17

Methods……..26

Figure Legend……...28

Figure 2……..30

Chapter 3: Nuclear Receptor Signaling in Relation to CDCs……...32

Methods……..43

Figure Legend……...48

Figure 3……..51

Chapter 4: Phospholipid Metabolism in Relation to CDCs and Group A Strep…….56

Methods……..63

Figure Legend……...68

Figure 4……..…69

Chapter 5: Discussion and Future Directions……71

References……77

Acknowledgements

It's difficult to imagine that it's been nearly 6 years since I have begun my Ph.D. program. I am a double Bruin, starting as an undergraduate initially majoring in Math and Economics in Fall 2013. Within the first week of my 1st year, I switched my major into Microbiology, Immunology, and Molecular Genetics, thinking it would be an appropriate pre-med major. But I abandoned my goals of pursuing a medical degree after realizing that I am dreadful when interacting with people. Instead, I chose to pursue biomedical research as a potential career choice after taking a course titled Biomedical Research 5HA with Dr. Rafael Romero. Fast forward 10 years, I am graduating with a Ph.D. in Molecular and Medical Pharmacology from an institution that honestly felt like a second home. During this journey, I have met some of most amazing individuals that I would like to highlight in this acknowledgement.

First and foremost, I would like to express my sincere gratitude to my research mentor, advisor, and colleague, Dr. Steven Bensinger. Even before my acceptance to UCLA Ph.D. program, I was always interested in studying the intersection between immunology and metabolism. After reading about Dr. Bensinger's research interest on lipid metabolism and immune cells, I immediately expressed my interest in joining his lab. We were discussing the top three ongoing projects at the time, and I honestly cannot describe the amount of passion I have felt. He was truly one of the most intelligent individuals I have met, and even to this day, I am amazed by his ability to critically think about a scientific problem and rapidly integrate multiple ideas to formulate a logical hypothesis. Dr. Bensinger has continuously challenged me to think outside the box and develop a sharp sense of skepticism, rather than blindly believing what is presented in front of me. I have acquired incredible amount of knowledge and value under his mentorship, and I will carry these soft skills throughout my entire career.

I would like to thank the members of my dissertation committee, Drs. Ting-Ting Wu, Jeff Miller, Elizabeth Tarling, and Phil Scumpia. Our first, collective meeting took place via Zoom for my ATC oral presentation, which also took place one day before 2020 election. It was certainly

a different world back then, and soon enough, we will likely be faced with a presidential rematch. Everyone in my committee provided very insightful feedbacks regarding my scientific intellect, approaches of asking new questions and approaching a new hypothesis, and presentation styles. They played a vital role in my scientific growth and development.

I would like to thank all my lab mates, former and present, who truly made lab feel like another family. Allison Chi, Dylan Zhou, and Wayne Hsieh were the senior members in the lab when I first joined in 2018. They were one of the biggest reasons why I wanted to stay in the lab. There has been many turnovers over the past 6 years, and I am thankful for every one of them for playing a vital role in helping shape my personal development. Eliza Kronenberger, Xen Hoi, Amy Vichaidit, Palik Joulakian, and Jonathan Quintana all have been phenomenal individuals, and I'm certain that they will achieve fantastic career goals. Ian Ford and Kelly Kennewick are my graduate student buddies, and we have struggled and grown together since the beginning of our Ph.D. career. We helped each other out whenever we needed, and I greatly appreciate the friendship that we have built over the past several years. Alessandro Sammarco, Tianheng Hou, and Richard Watson are the post-docs in the lab, and each of them provided genuine mentorship and support throughout my studies. Ali Kuhlmann and Chloe Qiao are newer members of our lab, and both have great passion and ambition. I'm sure both will become very successful scientists in their respective careers. While not officially part of Dr. Bensinger's laboratory, Kevin Williams and Gino Su have always fostered a friendly environment, and they have provided meaningful advice and scientific expertise when discussing about lipidomics data. My undergraduates—Austin Sun and Jarret Luk—also have played a great role not only in helping with my experiments, but an opportunity for me to provide meaningful mentorship. Finally, I would like to thank Margarita Calderon, who have been extremely supportive since the beginning of my Ph.D. program. No words can describe the amount of passion and joy that she has brought into our lab. Every time I felt mentally and

emotionally drained, her simple presence and smile melted away all my stress. She is an angel, and I will greatly miss her.

I would like to thank all the authors and collaborators who have helped shape my manuscript. Much of the infectious studies would not have been possible without the help of Kindra Scumpia. She also played a huge role in my personal development, providing great life advice and encouraging, mental support during my final stage of my Ph.D. career. Yajing Gao, JP Kennelly, Lijing Cheng, and Drs. Loren Fong, Peter Tontonoz, and Michael Wessels have provided great constructive feedback of my manuscript. I have quickly learned that science is a teamwork effort, and these collaborations are the reason that helped shape the manuscript that we have today.

I would also like to thank everyone else that I have met at UCLA. While I cannot list everyone's names, it has been an incredible journey meeting incredibly intelligent colleagues, many of whom have moved onto their careers. To highlight a few, I would like to thank Drs. Oliver Fregoso and Melody Li, along with my MIMG 102 teaching assistant colleagues, Serina Huang, Vivian Yang, Pablo Alvarez, and Karly Nissan, for an opportunity to learn about viruses and struggle together while grading midterms and leading discussion sessions. I would like to thank Shirley Zhang for the friendship and support during my Ph.D. program, along with a few small scientific discussions.

Lastly, I would like to extend my gratitude to my loving family and friends outside of my scientific community, who have always given unconditional love and emotional support. My church, Ecclesia, has not only nurtured my spiritual health, but also helped me cultivate an optimistic mindset. I've learnt extremely valuable life lessons, and I look forward to continue nourishing my relationship with the Holy Spirit. My girlfriend, Hannah, has been supportive of my Ph.D. career since the beginning of our relationship. Likewise, my mother has been my biggest support throughout my educational career, and I owe her lots.

Vita

EDUCATION:

B.S. in Microbiology, Immunology, and Molecular Genetics (UCLA), minor in biomedical research (2013-2017)

Ph.D. in Molecular and Medical Pharmacology (UCLA); 2018-present

SELECTED PUBLICATION

1. Zhou QD, Chi Xun, **Lee MS**, et al. Interferon-mediated reprogramming of membrane cholesterol to evade bacterial toxins. *Nature Immunology.* 21, 746-755 (2020).
2. **Lee MS** and Bensinger S. Reprogramming cholesterol metabolism in macrophages and its role in host defense against cholesterol-dependent cytolysins. *Cell and Molecular Immunology*. 19, 327-336 (2022).
3. Xiao Xu, Kennelly JP, … **Lee MS**, et al. Hepatic nonvesicular cholesterol transport is critical for systemic lipid homeostasis. *Nature Metabolism.* 5, 165-181 (2023).
4. Hong JS, Ahsan FM, … **Lee MS**, et al. CRTC2 regulates plasma cell metabolism and survival. *Biorxiv* (2021)
5. Yee KM, Shuai RW, … **Lee MS**, et al. TET1 controls Cxcl1 induction by DNA demethylation and promotes neutrophil recruitment during acute lung injury. *Biorxiv* (2021)

AWARDS & HONOR

1. NIH T32 Microbial Pathogenesis Training Grant (July 2019 to June 2020)
2. NIH T32 Microbial Pathogenesis Training Grant (July 2020 to June 2021)
3. UCLA Biomedical Research Minor Summer Fellowship (June 2016)
4. UCLA URFP J.W. & Nellie MacDowell Award (December 2015)

CONFERENCES AND PRESENTATIONS

1. **The American Association of Immunologists (AAI) Conference Poster Session || District of Columbia, Maryland**
    - **Poster title: *"Targeting Macrophage Cholesterol Homeostasis to Protect from Bacterial Pore Forming Toxins"* (May 2023)**

2. **UCLA Molecular and Medical Pharmacology Annual Retreat (November 2022)**
    - **Presentation title: "*Evaluating the Role of LXR Signaling in Mediating Host Defense against Bacterial Toxins*"**

3. **The American Association of Immunologists (AAI) Conference Poster Session || Portland, Oregon**
    - **Poster title: *"Targeting Macrophage Cholesterol Homeostasis to Protect from Bacterial Pore Forming Toxins"* (May 2022)**

4. **UCLA Immunology, Inflammation, Infection, and Transplantation Research Theme (I3T) Research in Progress Seminar || Los Angeles, California**
    - **Presentation title: "*Evaluating the Role of LXR Signaling in Mediating Host Defense against Bacterial Toxins*" (March 2022)**

5. **UCLA Molecular and Medical Pharmacology Annual Retreat || Santa Monica, California**
    - **Poster title: "*Reprogramming of Macrophage Cholesterol Metabolism to Attenuate Function of Bacterial Pore Forming Toxins"* (November 2021)**

6. Microbial Pathogenesis Training Grant Student Seminar || Los Angeles, California
    - Presentation title: *"LPCAT3 Mediated Phospholipid Remodeling Impacts Susceptibility to Pore-Forming Toxins"* (May 2021)

7. UCLA Molecular & Medical Pharmacology Annual Retreat || Huntington Beach, California
    - Poster title: *"Interferon-mediated Reprogramming of Plasma Membrane Cholesterol to Evade Bacterial Exotoxins"* (Nov 2019)

8. UCLA Undergraduate Science Poster Day || Los Angeles, California
    - Poster title: *"Epigenetic Regulation of CXCL1 in Response to NF-kB Activation"* (Summer 2016)

Chapter 1: Necrotizing Fasciitis, Group A Strep, and Cholesterol-Dependent Cytolysins

Necrotizing Soft Tissue Infections

Necrotizing fasciitis (NF), commonly known as “flesh-eating disease,” is a bacterial infection that results in severe necrosis of the body’s soft tissues (subcutaneous tissues and fascia) (*1-3*). Such necrotizing infections can occur after major traumatic injuries, as well as after minor breaches of the skin or mucosa. Significant morbidity and mortality will follow, should the patient not receive aggressive treatments. Antibiotic therapy is mandatory, and early surgical debridement is critical to maximize patient survival (*1, 2, 4*).

NF occurs in about 0.4 people per 100,000 annually in the United States, and about 1 per 100,000 in Western Europe (*5*). Both sexes are equally affected, and it is more common in older individuals than children. Early symptoms of NF may include fever, swelling, and excessive pain (*3*). Diagnosis is very difficult at earlier stages of the disease because NF is difficult to differentiate from cellulitis or other superficial skin infections. However, some signs that are more suggestive of necrotizing changes may start to appear in later stages. These signs include: formation of bullae, skin turning from red to purple and black due to thrombosis of the blood vessels, increased pain, presence of gas in tissues, and reduced sensation over the skin due to the necrosis of the underlying nerve tissues(*1, 6*).

Over 70% of documented cases of NF are found in patients who manifest at least one of these clinical situations: immunosuppression, diabetes, alcoholism, drug/substance abuse, smoking, malignancies, and chronic systemic diseases. These observations suggest that the pathogenesis of NF can be influenced by the patient’s immune and metabolic status, as well as lifestyle factors (*7-9*).

NF is characterized by either type I (polymicrobial) or type II (monomicrobial) infection. Type I NF is a polymicrobial infection, often associated with gas in the tissue, making it difficult to distinguish from gas gangrene. Type I NF is more common, accounting for 70-80% of cases. Various species of bacteria cause this type of infection, such as gram-positive cocci, gram-negative rods, and anaerobes (*9*). Population of those affected are typically older with medical

comorbidities, such as diabetes mellitus, immunodeficiency, and obesity. Type II monomicrobial infection is less common, and group A streptococcus is the most common pathogen that accounts for most type II NF cases (*5, 10, 11*).

Group A *Streptococcus Pyogenes* (GAS)

Group A streptococcus (GAS) are beta-hemolytic Gram stain -positive bacteria that can cause a wide range of disease from very mild to severe, and life-threatening (*12*). It is unclear what specifically predisposes different individuals to develop different disease outcomes from the same pathogen, but it is suspected that the host's phenotypic, genetic, and epigenetic factors are the source of variation (*9, 13*). Furthermore, these GAS microbes express multiple virulence factors, which can differentially influence the host's disease pathogenesis. Mild GAS infections include pharyngitis (strep throat), impetigo, and scarlet fever. Invasive GAS infections can result in severe organ failure, toxic shock syndrome (STSS), pneumonia, and of course, necrotizing fasciitis (*4*).

S. pyogenes employs key virulence factors that enable it to attach onto host tissues, evade the immune response, and spread by penetrating host tissue layers. Hyaluronidase facilitates bacterial spreading by breaking down hyaluronic acid, which is essential for connective tissue integrity (*7, 13*). Streptodornase is a DNase that protects bacteria from being trapped in neutrophil extracellular traps (NETs) by digesting the NET's web of DNA (*13*). M protein can inhibit opsonization by the alternative complement pathway by binding to host complement regulators (*14*). Serine protease, ScpC, prevents the migration of neutrophils to the spreading infection by degrading the chemokine IL-8, which serves as chemoattractant for neutrophils (*15*). In combination, these virulence factors play a pivotal role in the evasion of the immune system. Furthermore, *S. pyogenes* secrete two major types of pore-forming toxins: Streptolysin S (SLS) and Streptolysin O (SLO). SLS has been shown to induce hemolysis by targeting sodium-bicarbonate cotransporter NBCn1, as well as induction of NF-κB-activation in

keratinocytes (*16*). SLO is a cholesterol-dependent cytolysin (CDC) that relies on cholesterol availability in the host plasma membrane for pathogenesis (*17*).

Diet-induced dysregulation of lipid metabolism increases susceptibility to the development of necrotizing lesions in skin.

Diabetes and obesity are risk factors that predispose individuals to the development of necrotizing skin and soft tissue infections, including necrotizing fasciitis (NF), leading to the supposition that systemic dysregulation of lipid metabolic metabolism could underlie the development or severity of NF. To test the idea that diet-induced dysregulation of metabolic homeostasis would influence tissue destruction by invasive GAS infection, C57BL/6 mice were placed on a Western (WD), high-fat (HF) or control chow diet for 12 weeks. Mice were then challenged with intradermal injection of *S. pyogenes* (strain 854 M1 type), isolated from a patient with an invasive infection (*18, 19*). Mice were monitored for the development of ulceronecrotic lesions at the injection site. We observed that WD-fed mice universally developed larger skin ulcers than their HF- and chow-fed counterparts (**Fig. 1A, 1B**). Histologic examination of HF- and chow-fed mice revealed localized full thickness necrosis of the epidermis, dermis, and subcutaneous tissue (**Fig. 1C**). Edema, immune cell infiltrates, and bacteria were present in the subcutaneous tissue along with thrombosed blood vessels, histologic features observed in human necrotizing fasciitis (**Fig. 1C**). WD-fed mice displayed extensive areas of full thickness necrosis with spread of edema, immune cells, and bacteria well beyond the initial infection site (**Fig. 1C**). The concentration of bacteria per gram was similar across all experimental mice (**Fig. 1D).** Anecdotally, we found that the length of time that a mouse was on WD (i.e., 8 weeks versus 12 weeks) correlated with the severity of tissue damage in GAS infection (**Fig. 1E**). These data show that Western diet-induced changes specifically exacerbate skin tissue destruction caused by invasive GAS skin infection.

SLO-Deficient Group A Strep

Early studies have addressed the biological impact of SLO *in vivo* using either wild type (strain 950771) or SLO-deficient Group A Strep (strain 950771SmSLO) (*20*). Mice infected with these bacterial strains (subcutaneously or intraperitoneally), revealed that SLO-deficient GAS caused less mortality than wild type GAS. Likewise, a recent study have performed an intravenous infection with either wild type (*emm* type 1.0) or SLO-deficient GAS (*emm* type 32.2), and found that mice infected with SLO-deficient GAS survived 96h post-infection, while mice infected with wild type GAS succumbed to infection by 24h post-infection (*20*). The bacterial load in blood was also 3.5 log lower in the SLO-deficient GAS infection by 24h compared to wild type GAS infection (*21*).

The observation that mice fed a diet enriched for cholesterol resulted in increased tissue damage during GAS infection led us to ask if SLO was responsible for this increased sensitivity. To test this idea, WD- and chow-fed mice were challenged with intradermal wild type or SLO-deficient *S. pyogenes* (designated wt or ∆slo, respectively) (*22*). Mice were monitored for the development of ulceronecrotic lesions in the skin up to 96 h after intradermal challenge. We observed that lesion development and overall area was largely indistinguishable for WT or ∆SLO *S. pyogenes* infections in chow-fed mice (**Fig. 1 F, 1G**). In contrast, we found that the increased tissue damage observed in WD-fed mice was entirely dependent on SLO (**Fig. 1 F, 1G**). It remains unclear why SLO mediates damage in a context dependent manner (e.g., Western versus Chow diet). One logical hypothesis is that WD-fed mice have more cholesterol content in their tissues compared to chow diet-fed mice, and therefore, have increased sensitivity to CDC mediated damage. However, more studies are needed to better understand the crosstalk between WD and host immunity, as well as the how SLO facilitates microbial pathogenesis.

Using CDCs as a Reductionist Approach to Study Tissue Damage

We recognized that the difference in GAS pathogenesis in WD-fed mice was likely multi-factorial and could be secondary to alterations in innate immune cell function or other processes involved in antimicrobial host defense. Thus, we sought a reductionist system to ask if diet-induced changes in lipid metabolism intrinsically altered susceptibility to microbial toxins capable of inducing tissue necrosis. We have previously shown that intradermal injection of CDCs (*e.g.*, streptolysin-O (SLO) or anthrolysin-O (ALO)) induce necrotizing ulcers, providing a simplified system to test if diet-induced changes in lipid homeostasis would influence the development of tissue necrosis (*23*). SLO was directly injected into the dermis of mice fed WD or chow for 8 weeks, and ulcers were measured over 72 h. Similar to our results with *S. pyogenes* skin infections, WD-fed mice developed markedly larger ulcers than their chow-fed counterparts **(Fig. 1H, 1I).** Interestingly, mice fed a high fat (HF)-diet that lacked cholesterol had similar lesion area to that of chow-fed mice following toxin administration **(Fig. 1H, 1I)**, suggesting a causal requirement for cholesterol in the diet. Histological analysis confirmed that WD-fed mice displayed larger areas of necrosis compared to chow-diet, while HF-fed mice displayed an intermediate level of necrosis between that of chow- and WD-fed mice **(Fig. 1J, 1K).** Diet time-course studies revealed that mice required a minimum of 6 weeks on WD before differences in lesion sizes induced by CDCs were observed **(Fig. 1L).** Mice fed with either HF-diet or WD showed similar weight at 8 weeks, indicating that the heightened susceptibility to SLO in WD-fed mice was not due to enlarged body mass alone **(Fig. 1M).** Thus, a specific alteration driven by a WD-diet rather than obesity or immune dysfunction caused by obesity *per se* is an underlying host factor that influences the pathogenesis of necrotizing lesions to CDC pore-forming toxins.

CDC's Mechanism of Action

CDCs are virulence factors secreted by a wide range of gram-positive (and one gram-negative) bacteria that can cause many different diseases. All pathogenic clinical isolates of *S. pyogenes* produce the CDC, streptolysin O (SLO), and the deletion of SLO from S. *pyogenes* attenuates bacterial virulence in murine models (*24*). Likewise, most pathogenic isolate of *S. pneumoniae* produces the CDC, pneumolysin (PLY), and the deletion of PLY from *S. pneumoniae* attenuates bacterial virulence (*24, 25*). *L. monocytogenes* relies on its CDC toxin, listeriolysin O (LLO), to escape cellular vacuoles and can cause meningitis and miscarriage, while *C. perfringens* rely on its CDC toxin, perfringolysin O (PFO), to cause gas gangrene (*24, 26*).

The molecular structure of CDC consists of 4 domains. Domains 1 and 2 play a structural role, while Domain 3 (D3) enables the molecule to initiate oligomerization into a pre-pore intermediate. Domain 4 (D4) is the region that enables CDC to recognize and bind into cholesterol embedded in a target cell membrane, hence the name, “cholesterol-dependent” cytolysin (*17, 27*). CDCs are secreted as a soluble monomer that binds into host cell membrane via D4, and following binding, the toxin monomers oligomerize into a pre-pore intermediate composed of ~30-50 monomers (*27*). After pre-pore formation, each monomer undergoes coordinated conformational change to refold each transmembrane helices into membrane-spanning β-strands, which ultimately forms a β barrel in the membrane, resembling a pore. Formation of these pores cause ion flux (Ca^{2+} influx and K^{+} outflux), as well as loss of cellular ATP and essential proteins (*24*).

Many biological systems exhibit an “all-or-none” type of cellular responses. A well-known example of this phenomenon occurs during the firing of action potential. The opening of sodium channels enables rapid influx of sodium ions into the cells, leading to membrane depolarization. However, an action potential will not fire unless intracellular voltage reaches above a certain threshold potential. Similarly, cholesterol sensing machinery show a strong sigmoidal response. Biochemical studies have shown that truncated versions of cholesterol dependent cytolysins

(i.e., retains cholesterol binding activity but fail to oligomerize into pores) exhibit sigmoidal binding kinetics, as opposed to a linear, concentration-dependent response. The sigmoidal response of these cholesterol sensors could rise either due to positive cooperativity or limited cholesterol availability in the plasma membrane (*28*).

One of the explanations as to why SLO-deficient GAS was unable to cause profound tissue damage in WD-fed mice (compared to WT GAS) could be attributed to this "all-or-none" phenomenon. WD contains heightened cholesterol content, which presumably becomes distributed across all of the animal's tissues. It could be possible that WD-fed mice contain cholesterol that is above a certain threshold for CDC binding to target cells, which consequently enables SLO to cause tissue damage. Conversely, chow-fed mice may not contain sufficient cholesterol content, which is why there is no significant lesion differences between WT vs. SLO-deficient GAS infection. However, these observations are still premature, and more rigorous studies need to be performed to address these concerns.

Cellular Consequences of CDCs

The primary outcome of CDC binding is direct cellular lysis due to osmotic imbalance. However, the relative amount of cellular lysis depends on the target cell type. For instance, red blood cells are much more sensitive to lysis than other cell types such as macrophages and myocytes because they lack the ability to undergo membrane repair (*29*). Furthermore, different CDC molecules bind and alter membrane integrity differently. In our studies with bone marrow-derived macrophages (BMDMs), PFO, SLO, and ALO display different cytotoxic kinetics (*24*). Both PFO and ALO leads to near 100% loss of membrane integrity within 1 hour, while SLO takes over 4 hours to cause on average, 80% loss of membrane integrity. Other current studies in dermal fibroblasts, human umbilical vascular endothelial cells (HUVEC), and MLE-12 lung epithelial cells display similar loss of membrane integrity kinetics when PFO is used at an

increased concentration, suggesting that different cell types exhibit differential sensitivity to CDCs.

Increased resistance to CDCs observed in nucleated cells could be attributed to membrane repair mechanisms. Upon CDC-mediated pore formation, Ca^{2+} ions can flow into the cells and target various membrane repair pathways, such as patch repair, clogging, intrinsic repair, and endocytosis (*24, 30*). Both patch repair and clogging involve the recruitment of either internal vesicles or annexins that form a patch to reseal the damaged membrane. Intrinsic repair involves the "shedding" of the damaged membrane in the form of microvesicles (*31*). Endocytosis helps remove the toxin-bound membranes via internalization.

In addition to direct cellular lysis, CDC-mediated cellular damage can activate the MAPK pathways via Ca^{2+}/K^{+}-mediated activation of p38. Activation of p38-dependent MAPK can promote host survival via production of pro-inflammatory cytokines (e.g., IL-8, TNF-α, and IL-6) (*24*). as well as the activation of unfolded protein response (UPR), a stress response that upregulated protein chaperones in the endoplasmic reticulum (ER) (*32*). It has been shown that PLY can inhibit p38-mediated MAPK signaling via activation of a deubiquitinating enzyme, cylindromatosis, causing increased vascular leakage and acute lung injury.

CDCs target the "metabolically active pool" of plasma membrane cholesterol

Recent biochemical studies have shown that cholesterol content in the plasma membrane is unevenly distributed. There appears to be several distinct "pools" of cholesterol in the plasma membrane, each serving unique roles in PM structure and function. These cholesterol pools have been identified using purified Domain 4 of CDCs (e.g., ALO-D4), and it is thought that CDCs specifically target a rather small pool of cholesterol in the PM (*33, 34*).

This pool that is targeted by CDCs is described as the "metabolically active cholesterol pool." It is rather small, and the pool size can be rapidly altered in response to changes in total intracellular cholesterol concentration. It is thought to be in direct equilibrium with the cholesterol

sensing apparatus in the endoplasmic reticulum. For instance, a loss-of-function model in a gene called SREBP cleavage-activating protein (SCAP), which is essential for maintaining *de novo* cholesterol biosynthesis, has been shown to drastically reduce the size of the metabolically active cholesterol pool (*23*). Likewise, a pharmacological addition of simvastatin, which reduces cholesterol biosynthesis via direct inhibition of the enzyme, 3-hydroxy-3-methylglutaryl-CoA reductase (HMGCR), also has been shown to reduce the size of the metabolically active cholesterol pool (*23*). The exact distribution of this pool in the PM remains unknown, and further work is needed to determine its spatial location.

Another cholesterol pool in the PM is tightly associated with sphingomyelin (SM) and other phospholipid (PL) species. This pool is labeled as SM-sequestered pool, and the tight association of cholesterol with SM forms the biophysical basis for the assembly of lipid microdomains (commonly known as lipid rafts). This distinct cholesterol pool can be recognized using a fungal-derived protein, osterolysin A (OlyA) (*34, 35*). Unlike the metabolically active pool, SM-sequestered pool is not thought to directly communicate with the cholesterol-sensing machinery in the ER. However, when cells are treated with *S. aureus*-derived sphingomylinease (SMase), an enzyme that hydrolyzes sphingomyelin into ceramides and phosphocholine, decreases OlyA binding and increases the size of the metabolically active pool (*23*).

During gas gangrene, PFO has been shown to act synergistically with another *C. perfringens* virulence factor, α-toxin. This α-toxin possesses a phospholipase function by cleaving phosphatidylcholine and sphingomyelin, which liberates cholesterol from SM-sequestered pool and enhance PFO activity (*24, 36*). PFO and α-toxin together can thus subvert the host immune response by limiting the extravasation of inflammatory cells into the site of infection by destroying them. This cooperativity between CDCs and α-toxin is one example of a polymicrobial-like infection during necrotizing fasciitis.

The remaining cholesterol appears to exist in a third pool, known as the essential pool. Its size appears to be equivalent with the SM-sequestered pool, but its exact nature remains poorly understood. It is hypothesized that this essential pool is vital for the biophysical properties and bilayer integrity of the PM through its ability to foster molecular interactions between different classes of PL (i.e., PC, PS, PI, and PE) (*33, 34*). Unlike the metabolically active and SM-sequestered pool, no microbial product has been identified to be specifically target the essential pool nor exploited by pathogens to facilitate their lifecycle.

Methods

Dietary Models: WT C57BL/6 female mice at 8-weeks-old were fed on standard chow diet, high fat diet (45% kcal fat, Research Diet, D12451; composition available at https://www.researchdiets.com/formulas/d12451) or western diet (0.15% cholesterol, Research Diet, D12079B; composition available at https://researchdiets.com/formulas/d12079b) for indicated time.

Preparation of S. pyogenes culture: *S. pyogenes* strain: GAS 854 (*18, 19*) was provided by Dr. Michael Wessels (Boston Children's Hospital). GAS was grown overnight in THY broth at 37°C Celsius, 5% CO_2 incubator (*18, 19*). In the morning, a subculture (O.D. of 0.1) in THY broth was started and grown for 4hrs until the O.D. reaches between 0.65 – 0.7 (Approximately 2 x 10^8 cfu/mL). Bacteria was spun down at 800 g for 15 mins, washed once with PBS, and resuspended in 1 mL PBS (Approximately 5 x 10^6 CFU in 50 μL). Titers were confirmed by plating serial dilutions on blood agar plates.

In vivo S. pyogenes infection**:** Experimental mice fedwere shaved on the lower back and were intradermally injected with 5 x 10^6 cfu *S. pyogenes.* 96 h later, photographs of the skin wounds were taken and lesion area (cm^2) was measured using the ImageJ software. Wounds were excised for histological analysis and bacteria burden studies.

In vivo SLO injection**:** All *in vivo* SLO injections were performed as previously described (*23*). Mice fed on chow, high-fat (HF), and WD were shaved on the lower back and were intradermally injected with either PBS or SLO (8 kU/mouse). SLO was activated with 10 mM DTT at room temperature. 72 h later, photographs of the skin lesions were taken, and the lesion area (in cm^2) was measured using the ImageJ software.

Bacterial load determination: Mice were euthanized by CO2 inhalation and rapidly used for tissue dissection. During necropsy of mice, injection site tissue including epidermis, dermis, and subcutaneous tissue were dissected and weighed. Tissues were then transferred to 2 mL eppendorf tubes containing 5 mm stainless steel beads (QIAGEN, Cat# 69989) and 1 mL of ice-cold sterile distilled water. Tissues were homogenized using a TissueLyser II (QIAGEN) for 10 min at 30 Hz. To determine bacterial load recovery, serial dilutions were made and plated on TSA plates with 5% Sheep Blood plates (Fisher Scientific, Cat# R01198), and colonies were counted after overnight incubation at 37°C with 5% CO2.

Histology: Skin was fixed overnight in 10% neutral buffered formalin followed by standard histologic processing. H&E stained slides were evaluated by a board certified dermatopathologist. Histologic ulceration scores were determined according to the following scale: 0 – no ulceration/ erosion (only dermal inflammation and edema, 1- erosion, 2- erosion/ulceration, 3- epidermal ulceration, 4 – epidermal and dermal ulceration, 5 – full thickness ulceration of epidermis, dermis, and panniculus.

Figure Legend

Fig. 1 || (A,B) Representative images and lesion area from mice fed with chow diet, western diet (WD), or high-fat diet (HFD) for 13 weeks and then challenged with intradermal *S. pyogenes* (strain 854 M1 type, 5 x 10^6 CFU per mouse) for 96h. Lesions are marked with white arrow. **(C)** Representative photomicrographs of H&E stained wound sections from chow diet-, WD-fed, and HFD-fed mice infected with intradermal *S. pyogenes* (as above in **A,B**)**.** Gray dashed line=ulceration. Scale=1000μm (**D**) Bacterial load (CFU/mg tissue) cultured from wounds of chow diet-, WD-fed, or HFD-fed mice after *S. pyogenes* injection. **(E)** Lesion area from mice fed with chow diet or WD for either 9 weeks or 13 weeks, followed by intradermal *S. pyogenes* challenge for 96h. **(F,G)** Representative images and lesion area from mice fed with chow diet or WD for 13 weeks and then challenged with intradermal *S. pyogenes* (strain 854 M1 WT or ΔSLO, 5 x 10^6 CFU per mouse) for 96h. Lesions are marked with white arrow. **(H, I)** Representative images and lesion area from chow-, high fat (HF)-, or WD-fed mice challenged with intradermal streptolysin-O (SLO; 8 kU/mouse) for 72h. Lesions are marked with white arrow. **(J)** Representative photomicrographs of H&E stained wound sections of chow-, WD- or HF-fed mice 72 hours after intradermal SLO injection. Yellow dashed line=erosion, gray dashed line=ulceration. Scale=500μm. **(K).** Histologic ulceration scoring from mice fed chow-, Western diet (WD) or high fat (HF) for 8 weeks and then challenged with intradermal SLO (8 kU/mouse) for 72h as in Fig 1H. **(L)** Quantification of SLO-induced lesion size from mice from mice fed chow- or WD-diet for 4-weeks, 6-weeks, or 8-weeks then challenged with intradermal SLO (8 kU/mouse) for 72h as above. **(M)** Quantification of body weight of mice fed in either chow-, WD-, or HF-diet for 8-weeks.

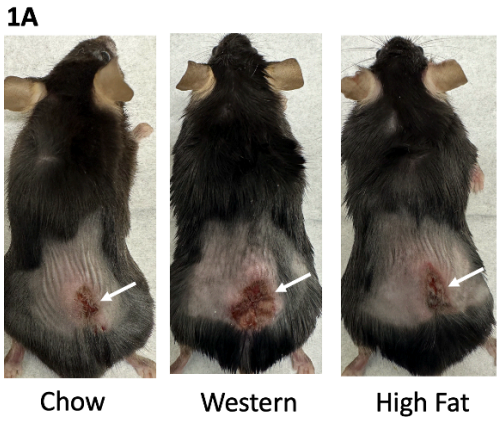
1A
Chow
Western
High Fat

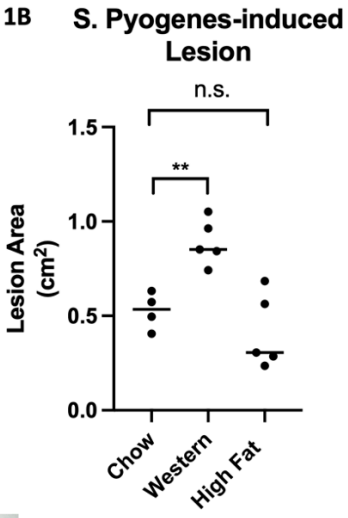
1B
S. Pyogenes-induced Lesion
n.s.
**
Lesion Area (cm2)
1.5
1.0
0.5
0.0
Chow
Western
High Fat

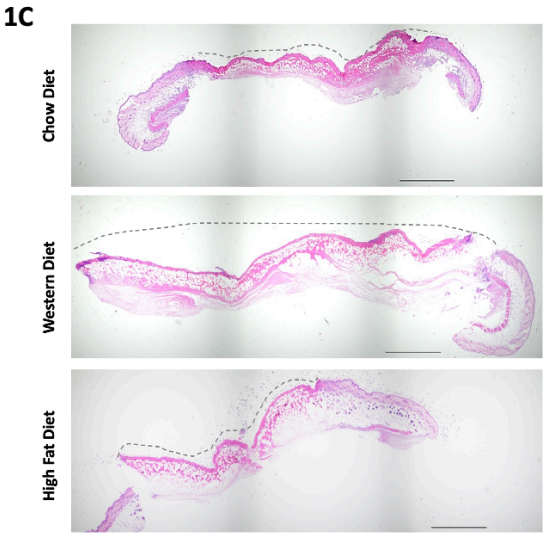
1C
Chow Diet
Western Diet
High Fat Diet

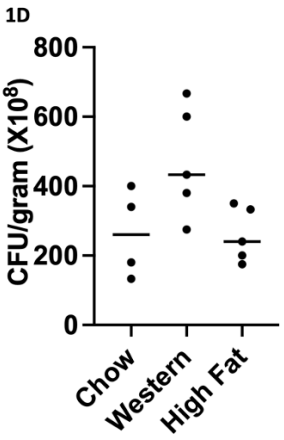
1D
CFU/gram (X10^8)
800
600
400
200
0
Chow
Western
High Fat

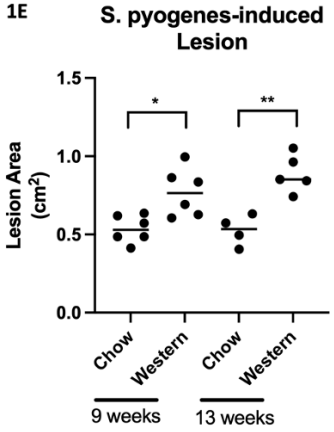
1E
S. pyogenes-induced Lesion
*
**
Lesion Area (cm2)
1.5
1.0
0.5
0.0
Chow
Western
Chow
Western
9 weeks
13 weeks

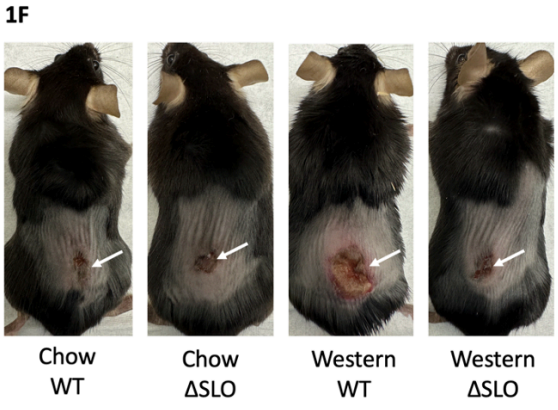
1F
Chow WT
Chow ΔSLO
Western WT
Western ΔSLO

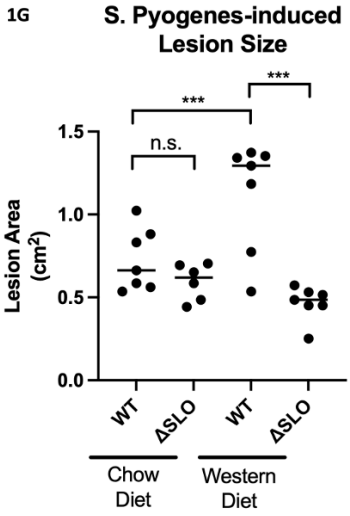
1G
S. Pyogenes-induced Lesion Size
***
***
n.s.
Lesion Area (cm2)
1.5
1.0
0.5
0.0
WT
ΔSLO
WT
ΔSLO
Chow Diet
Western Diet

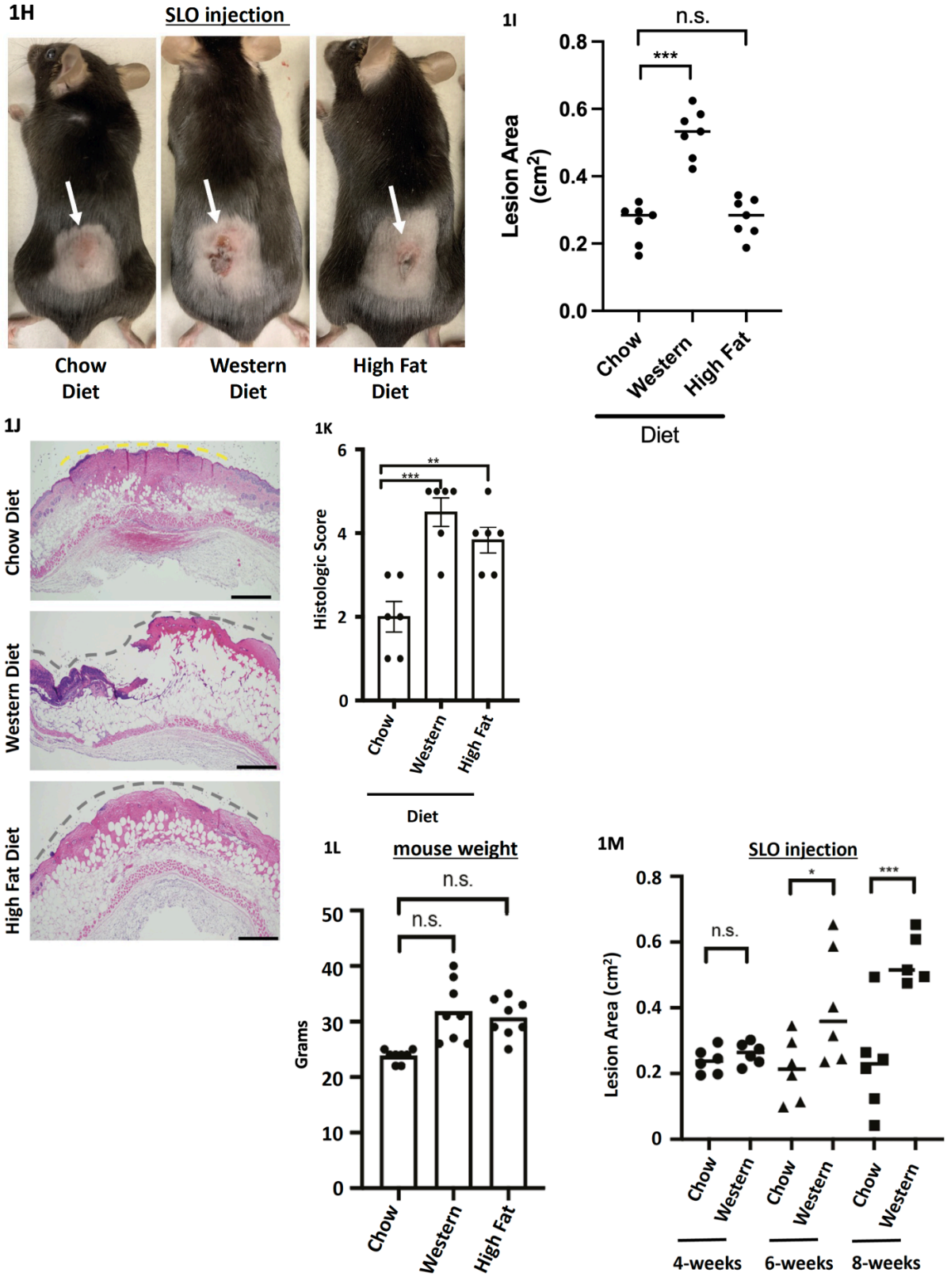
1H
SLO injection
Chow Diet
Western Diet
High Fat Diet
1I
n.s.
***
Lesion Area (cm²)
0.8
0.6
0.4
0.2
0.0
Chow
Western
High Fat
Diet
1J
Chow Diet
Western Diet
High Fat Diet
1K
**
***
Histologic Score
6
4
2
0
Chow
Western
High Fat
Diet
1L
mouse weight
n.s.
n.s.
Grams
50
40
30
20
10
0
Chow
Western
High Fat
1M
SLO injection
n.s.
*
***
Lesion Area (cm²)
0.8
0.6
0.4
0.2
0
Chow
Western
Chow
Western
Chow
Western
4-weeks
6-weeks
8-weeks

Chapter 2: Cholesterol Homeostasis and CDC activity

Regulation of Cellular Cholesterol Homeostasis

Cholesterol is the most abundant lipid species found in mammalian cells, accounting for up to 30% of total lipids (*37*). Cholesterol can either be synthesized within cells or directly imported via internalization of lipoproteins. Unlike many lipid species, cholesterol cannot be degraded by mammalian cells, and thus, excess cholesterol is either stored in intracellular depots as lipid droplets or exported out of the cell via cholesterol efflux pathways (*34, 37*). Disrupted regulation of cholesterol metabolism is associated with many types of severe congenital disease, such as Tangier's disease, familial hypercholesterolemia, Niemann-Pick type C disease, and Schnyder corneal disease. Therefore, it is crucial that cells maintain intricate mechanisms to regulate cholesterol homeostasis.

Cholesterol Synthesis

Cholesterol is synthesized through enzymatic activity of over 20+ distinct metabolic steps in the mevalonate pathway and the downstream of cholesterol synthesis pathway. As stated in the previous section, the biochemical machinery that regulates cholesterol synthesis is found in the smooth endoplasmic reticulum membrane, and each of these enzymes are subject to multiple layers of posttranslational modifications to ensure tight control over synthetic capacity and import to avoid deleterious accumulation (*37*).

The expression of cholesterol biosynthetic enzymes is transcriptionally regulated by the transcription factor, sterol regulatory element-binding protein 2 (SREBP2). Upon cholesterol-replete conditions, SREBP2 is held in the ER, effectively reducing cholesterol synthesis. When cholesterol content falls below a threshold, SREBP2 translocates to the Golgi body, where its nuclear domain becomes sequentially cleaved. Cleaved SREBP2 then moves to the nucleus to transactivate genes encoding enzymes in the cholesterol synthetic program (*37-39*).

One target gene of SREBP2 is the gene encoding for the rate-limiting enzyme of cholesterol synthesis, HMGCR. Increased amounts of oxysterols in the ER, such as 25-

hydroxycholesterol (25HC), can induce the degradation of HMGCR, resulting in decreased cholesterol synthesis. The production of 25HC can be induced by the enzymatic activity of cholesterol 25-hydroxylase (CH25H), which converts cholesterol into 25HC (*37*). Interestingly, CH25H is classified as an interferon-stimulated gene (ISG), particularly in the context of antiviral response. The IFN-mediated upregulation of CH25H-dependent production of 25HC appears to underlie many of the changes in cholesterol homeostasis observed in macrophages during inflammatory response to viruses and some microbes (*40*).

Cholesterol Import

A bulk of the intracellular cholesterol content is maintained via utilization of cholesterol import pathways. Cholesterol import canonically occurs via the internalization of low-density lipoproteins (LDL) from the extracellular space via low-density lipoprotein receptor (LDLR). LDLR is also a transcriptional target of SREBP2, implying that when cells upregulate cholesterol synthetic pathways, they can also increase cholesterol import. Extracellular surface of LDLR captures circulating LDLs from the bloodstream, and these LDL particles become subsequently internalized via clathrin-coated vesicles (*37, 41*). Following endocytosis, LDL-carried cholesterol esters (CE) are hydrolyzed by lysosomal acid lipases in the lysosomes, liberating free cholesterol. These cholesterols are then exported from the lysosomal lumen via the concerted actions of Niemann-Pick Type C1 (NPC1) and NPC2, and they're ultimately delivered to other subcellular compartments, such as the ER and PM (*37*).

Cholesterol Export

Unlike other lipid metabolites, mammalian cells do not have a built-in catabolic pathway that can salvage cholesterol into smaller monomers. Instead, excess cholesterol is either exported out of cells via efflux machinery or stored as cholesterol esters in lipid droplets. Cholesterol efflux pathways are transcriptionally controlled by lipid-dependent nuclear receptors,

liver X receptors (LXRα and LXRβ). Upon excess cholesterol accumulation, LXRs transactivate the genes, ATP-binding cassette transporter 1 (ABCA1) and ATP-binding cassette subfamily G Member 1 (ABCG1) to release cholesterol out of the cell (*42, 43*). It is thought that ABCA1 flips phospholipids and cholesterol from the inner to outer leaflet, which then allows apolipoproteins (e.g., Apo-A1) to "pick-up" these accumulated cholesterols (*37*). In contrast, ABCG1 is expressed intracellularly, and it facilitates the movement of cholesterol from the ER to inner leaflet via endosomal vesicles (*37*).

Both SREBP2 and LXR activities help establish cholesterol homeostasis inside cells. It is important to note that cellular signals, whether they're pro-inflammatory or anti-inflammatory, can differentially influence the activity of SREBP2 and LXR to support effector function (Discussed in the next section). **Fig 2A** shows a summary of the opposing transcriptional programs of SREBP2 and LXR that ensure cholesterol homeostasis in cells (*34*).

Cholesterol Esterification

Cholesterol esterification is another important mechanism of storing excess cholesterol in the form of cholesterol esters (CE) in lipid droplets. Two major isozymes regulate cholesterol esterification: acyl coenzyme A: cholesterol acyltransferase 1 (ACAT1) and ACAT2. ACAT enzymes utilize free cholesterol as an allosteric activator and a substrate, subsequently conjugating fatty acyl-CoA into the hydrophobic end of the cholesterol molecule (*37, 44*). Most common forms of CEs are CE 16:0, CE 18:1, and CE 22:4. Interestingly, neither ACAT1 nor ACAT2 is subject to transcriptional control by SREBP2 and LXR. Instead, both ACATs are upregulated by pro-inflammatory stimulus, including interferons and tumor necrosis factor (*44*), suggesting that cholesterol esterification play a useful role in controlling inflammation and host defense.

Cholesterol Trafficking

Due to cholesterol's largely hydrophobic nature, it is imperative that cells possess various strategies to traffic cholesterol between the aqueous, subcellular compartments. Cholesterol can be pulled out of the phospholipid bilayer into the cytoplasmic compartments via lipid-transfer proteins (LPTs) that contain hydrophobic cavity that conceals cholesterol from water. One example of a LPT is the oxysterol-binding protein (OBSP), which transfers cholesterol from ER membranes to the trans-Golgi network, as well as the late endosomes/lysosomes (*45*).

The accumulation of cholesterol in the metabolically active cholesterol has been shown to be recognized by Aster/GramD1 proteins. Aster A/B/C proteins are essential ER-proteins that promote non-vesicular transport of cholesterol from PM to ER (and vice versa). The GRAM domain of Asters interacts with phosphatidylserine (PS) that are enriched within the inner leaflet of the PM, while the StART domain facilitates cholesterol removal and transport from PM to ER (*46, 47*). It is thought that once the PM's inner leaflet cholesterol concentration reaches 5 mol% (the same composition that the SCAP-SREBP complex tries to maintain), Aster begins to transfer those excess cholesterol away from PM to ER (*46*).

Cholesterol Homeostasis in relation to CDC pathogenesis

As stated in the previous section, CDCs have been shown to target the cholesterol found in the small, "metabolically active pool." This cholesterol pool is also in direct communication with the ER, where most of the cholesterol homeostatic sensing machinery resides (e.g., SREBP, SCAP, HMGCR, ACAT, etc.). Therefore, one can hypothesize that the manipulation of intracellular cholesterol homeostasis can alter susceptibility to CDCs. Studies in the Bensinger laboratory have indeed shown this, demonstrated in the *Nature Immunology (2020)* paper by Zhou et al (*23*).

In order to address this hypothesis, the Bensinger laboratory leveraged two independent, but also interdependent assays. The first assay is the "CDC permeabilization live-

imaging assay." In short, cells (e.g., BMDMs, dermal fibroblasts, HUVECs, neutrophils, etc.) are stimulated with a cytokine or pharmacological agent for a certain time period, and they are challenged with a CDC toxin (e.g., PFO, SLO, or ALO) in the presence of propidium iodide (PI) and Hoechst. We can quantify the percent abundance of PI influx by calculating total number of PI+ cells divided by total Hoeschst-positive cells.

Additionally, we can measure the amount of "metabolically active" cholesterol content by utilizing a fluorescently tagged probe called ALO-D4. As mentioned above, "D4" is the 4th domain of a CDC molecule that recognizes and binds to PM cholesterol. A purified ALO-D4 will retain its ability to bind cholesterol but fail to properly oligomerize into a pore. Therefore, ALO-D4 is a useful, complementary assay that enables us to evaluate whether a change in membrane integrity due to differential PI influx is correlated to changes in ALO-D4 binding into the plasma membrane (*48*).

Indeed, my studies have shown that perturbations in cholesterol homeostasis can influence the degree of the loss of membrane integrity and CDC binding. When BMDMs were stimulated with simvastatin, a pharmacological agent that leads to decreased cholesterol synthesis, BMDMs showed increased protection from PFO, indicated by reduction in PI+ cells **(Fig 2B).** Likewise, ALO-D4 staining in simvastatin-treated BMDMs were lowered, suggesting that the abrogation of cholesterol synthesis is a protective attribute to CDC-mediated pathogenesis **(Fig 2C).** Similarly, treatment of BMDMs with 25HC also have shown increased protection from PFO, SLO, and ALO-mediated loss of membrane integrity, as well as near complete abrogation of ALO-D4 staining **(Fig 2D).** Finally, a genetic ablation of CH25H has led to increased susceptibility to CDCs both *in vivo*, as well as increased ALO-D4 staining **(Fig 2E, 2F).** These observations illustrate that *de novo* cholesterol biosynthetic machinery can be targeted for potential therapeutic applications against CDC-dependent bacterial pathogenesis, such as necrotizing fasciitis.

Follow-up studies targeting different arms of cholesterol homeostatic machinery have been performed to further solidify the relationship between the metabolically active cholesterol pool versus CDC-binding. We have also shown that a pharmacological inhibition of ACAT using S9318 led to increased susceptibility to CDCs and increased ALO-D4 binding **(Fig 2G, 2H)**. By blocking the formation of cholesterol esters, it is likely that free cholesterol remained in membranes targeted by CDCs,. The inhibition of cholesterol import using LDLR-deficient BMDMs display similar phenotype to that of simvastatin-treated cells—reduced susceptibility to CDCs and abrogated ALO-D4 staining **(Fig 2I, 2J).** Importantly, LDLR-deficient BMDMs can be "rescued" by the addition of acetylated-LDL particles, which enables cells to receive LDL-derived cholesterol independent of LDLR. Finally, BMDMs that are deficient in both ABCA1 and ABCG1 transporters have shown increased susceptibility to CDCs, as well as increased ALO-D4 binding **(Fig 2K, 2L).** This is likely because the absence of cholesterol efflux pathways allows free cholesterol to redistribute throughout various subcellular compartments, including the metabolically active pool of PM cholesterol. Altogether, these observations reinforce the relationship between alterations to intracellular cholesterol homeostasis and sensitivity to CDC-mediated pathogenesis.

Signal-Specific Reprogramming of Cholesterol Metabolism

It is well-understood that many types of immune cells reprogram their cholesterol metabolism in response to activation signals cytokines or danger signals (i.e., pathogen-associated molecular patterns (PAMPs)). Activation of naïve T-cells with IL-2 or PMA and ionomycin results in coordinated upregulation of both cholesterol biosynthesis and lipoprotein import to meet the anabolic requirements associated with growth and proliferation (*34*). During viral infection, it has been shown that cells upregulate CH25H, which produces 25HC that serves as a physical blockade that prevents viral entry (*40*).

Lipidomics and isotope tracer studies have revealed that macrophages rapidly upregulate cholesterol synthesis when activated with a MyD88-dependent pattern recognition receptors (PRRs), such as Toll-like receptor (TLR)-2, 7, and 9, as well as IL-1β receptor. This also leads to a general accumulation in total cholesterol, which implies that SREBP2 reprogramming is hitting both cholesterol synthesis and import pathways in response to these stimuli (See Chapter 3). The exact mechanism linking MyD88 signaling with SREBP2 has not been fully elucidated, but it is dependent on AKT/mTOR, and the transcription factor, NRF2 (*34, 49*).

In contrast, interferon (IFN) signaling and PRRs that generate an IFN response (e.g., Toll-like receptor 3-TRIF signaling, cGAS-STING signaling, MAVS and RIG-I signaling) downregulate cholesterol synthesis and increase cholesterol esterification (See Chapter 3). However, it is interesting to note that IFN-signaling does not alter total levels of cholesterol (*23*). This suggests that IFN signaling is specifically targeting the cholesterol biosynthetic arm (via upregulation of CH25H-dependent 25HC production) but retains total cholesterol levels by preserving cholesterol import or reducing cholesterol efflux.

The correlation between cholesterol synthesis and total cholesterol levels have yet to be determined. Both MyD88 and TRIF-IFN-dependent signaling have been shown to only target the metabolically active cholesterol pool, without disturbing the SM-sequestered cholesterol pool. Because the metabolically active pool is in direct equilibrium with the cholesterol biosynthetic machinery in the ER, it isn't surprising that changes in ALO-D4 staining is directly correlated to changes in net synthesized cholesterol in response to these signals. In other words, MyD88-dependent signaling results in increased ALO-D4 staining, directly corresponding to increased cholesterol synthesis, while TRIF-IFN signaling results in decreased ALO-D4 staining as well as reduced cholesterol synthesis.

Changes in the metabolically active pool is very subtle compared to the total cholesterol content, and therefore, it is not surprising that TRIF-IFN signaling leaves total cholesterol

unchanged. By targeting a very small cholesterol pool, the cells can maintain most of their total cellular cholesterol and preserve their effector functions. Perhaps this mechanism of TRIF-IFN-dependent reduction in cholesterol synthesis could be an evolutionary strategy to limit the amounts of metabolites from the mevalonate/isoprenoid/sterol pathways that could used by viruses for a growth advantage. Conversely, MyD88-dependent increase in cholesterol synthesis and import could provide another layer of host defense advantage against certain Gram-negative bacterial infections that trigger TLR 2,7, and 9. Altogether, this reciprocal relationship between MyD88 and IFN signaling in cholesterol homeostasis supports the concept that rapid and profound regulation of cholesterol homeostasis is an integral aspect of cell's ability to respond to a broad array of pathogens and inflammatory stimuli.

Methods

***Mouse strains**:* All WT mice were purchased from The Jackson Laboratory: WT C57BL/6 (JAX 000664), B6;129S6-*Ch25h*^{tm1Rus}/J (*Ch25h*$^{-/-}$, JAX 016263), LDLR KO, Lysm-cre ABCA1$^{-/-}$ ABCG1$^{-/-}$ mice were a kind gift from Dr. Elizabeth Tarling (UCLA).

***Cells**:* Bone marrow was differentiated into macrophages in DMEM containing 10% v/v FBS (HyClone, GE SH3007103), 5% v/v M-CSF conditioned media, 1% v/v pen/strep, 1% v/v glutamine (Invitrogen) 0.5% v/v sodium pyruvate (Invitrogen) for 7-9 days prior to experimental use. Cells were changed to media with 5% FBS at the time of stimulation.

CDC Permeabilization Live Imaging. BMDMs were seeded 5 × 10^4/well on 96-well plates (E&K Scientific, EK-25090, Greiner). Cells were left for 2 days before stimulation. Cells were pretreated with various agonists for 2-24 h depending on the experiment. For live-cell imaging, culture media were replaced by 37 °C PBS with 0.05% BSA, 1 ug/mL propidium iodide (PI) (VWR, 80057-368) and 5 ug/mL Hoechst 33342 (ThermoFisher, H3570). Then cells were challenged by spiking recombinant PFO (final concentration 1 nM), gamma-irradiated SLO (final concentration 22 nM), or recombinant ALO (final concentration 1.5 nM), and plates were imaged every 10 min on Molecular Devices ImageXpress XL using a 20x Objective (Nikon Plan Fluor, 0.3 NA). SLO was activated with the addition of 10 mM DTT in room temperature for 10 min. Total (Hoechst 33342-positive) and permeabilized (PI-positive) cell number were assessed using MetaXpress Software with Powercore using the Multi-wavelength cell scoring module.

Preparation of Fluorescent ALO-D4. Cysteine-substituted ALO-D4 were incubated with Alexa-594 (Life Technologies) at 4 °C overnight in 50 mM Tris-HCl (pH 7.5) and 150 mM NaCl (1x TBS) containing 1 mM TCEP. Free dye was separated by extensive buffer exchange with 1x TBS in Amicon 10 kDa cut off concentrator (Millipore), and stored at 4 °C.

Binding of ALO-D4 to Cells. Cells were seeded 1.5 × 10^5/well on PDL-coated coverslips (Neuvitro, fisher NC0672873) on a 24-well plate. After stimulation, cells were incubated with ALO-D4, or OlyA as described before. Briefly, macrophages were washed three times for 10 min in PBS/Ca/Mg containing 0.2% (wt/vol) BSA. Cells were then incubated with ALO-D4, OlyA (all 20 ug/mL) in PBS/Ca/Mg containing 0.2% (wt/vol) BSA for 2 h at 4 °C. Unbound proteins were removed by washing with PBS/Ca/Mg three times for 2 min each.

Confocal Microscopy Analysis. After fluorescently labeled ALO-D4 binding, cells were fixed with 3% paraformaldehyde for 15 min and stained with 5 mg/mL DAPI, then washed twice with PBS/Ca/Mg for imaging. Images were taken with an Axiovert 200M microscope and processed with Zen 2010 software (Zeiss). High-resolution images were taken by Zeiss LSM880 with Airyscan.

Quantification of Fluorescence Intensity. For signal quantification, cells were plated on 24-well plates (Cellvis, P24-0-N), treated, stained as above, and fixed cells in DPBS/Ca^{2+}/Mg^{2+} were imaged within 2 h. Images were taken at UCLA Molecular Screening Shared Resource core facility on a Molecular Device ImageXpress Confocal using a 20x Objective (Nikon Plan Fluor, 0.3 NA) on a Molecular Devices ImageXpress XL. Maximum projected cellular fluorescence intensity was assessed by MetaXpress Software with Powercore using the Multi-wavelength cell scoring module. Integrated fluorescent intensity profile were exported and analyzed by R with ggplot2 package.

Figure Legend

Fig 2 | (A) Diagram of the transcriptional programming of cholesterol homeostasis, split between Liver X Receptor (LXR) and SREBP2 pathways. **(B)** Percentage of propidium iodide (PI)-positive cells stimulated with either vehicle control or simvastatin (2.5 μM) for 24 h in the presence of PFO challenge. **(C)** Confocal images of macrophage cultures stimulated with simvastatin at select dosage (1, 2.5, and 5 μM) for 24 h and then stained with fluorescent ALO-D4 and DAPI, scale bar 10 μm, along with corresponding violin plots of cellular fluorescent intensity. **(D)** Percentage of PI-positive cells stimulated with vehicle or 25-hydroxycholesterol (25-HC. 3 μM) for 24 h in the presence of PFO challenge. **(E)** Representative lesion images of control or CH25H KO mice challenged with intradermal SLO (8 kU/mouse) for 48 h. Lesions are marked with white arrow. Representative histology from mice pictured in k demonstrates serum crust overlying partial thickness erosion with a small full-thickness ulceration (green dotted line) of the epidermis, and a robust inflammatory response in the dermis and adipose tissue in control (B6) mice (upper panel). Wound areas in CH25H-deficient mice demonstrate a large ulceration (green dotted line) with necrosis/destruction of the papillary and much of the reticular dermis with a less pronounced inflammatory response (bottom panel). Scale bar, 500 μm. **(F)** Confocal images of macrophage cultures of wild type or CH25H-deficiency background stained with fluorescent ALO-D4 and DAPI, scale bar 10 μm. **(G)** Percentage of PI-positive cells stimulated with either vehicle control or ACAT inhibitor, Avasimibe (4.3 μM) for 24 h in the presence of PFO challenge. **(H)** Violin plots of cellular fluorescent intensity from wild type macrophage cultures stimulated with either vehicle control or ACAT inhibitor, Avasimibe (4.3 μM) for 24 h. **(I)** Percentage of PI-positive cells of either wild type or LDLR KO macrophage cultures in the presence of PFO challenge. **(J)** Violin plots of cellular fluorescent intensity from wild type or LDLR KO macrophage cultures. **(K)** Percentage of PI-positive cells of either wild type or ABCA1/ABCG1 DKO macrophage cultures in the presence of PFO challenge. **(L)**

Confocal images of either wild type or ABCA1/ABCG1 DKO macrophage cultures stained with fluorescent ALO-D4 and DAPO, scale bar 20 10 μm, along with corresponding violin plots of cellular fluorescent intensity.

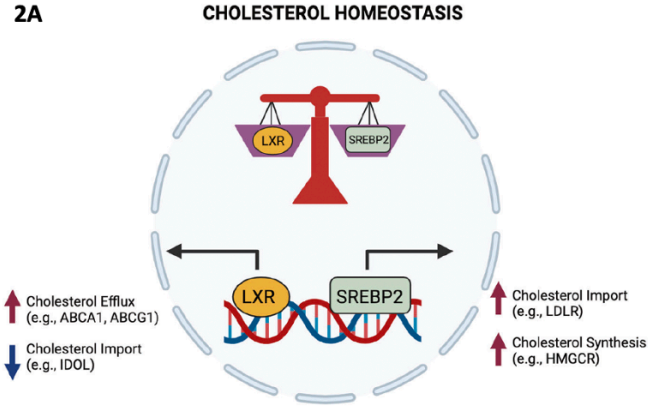
2A
CHOLESTEROL HOMEOSTASIS
LXR
SREBP2
LXR
SREBP2
Cholesterol Efflux
(e.g., ABCA1, ABCG1)
Cholesterol Import
(e.g., IDOL)
Cholesterol Import
(e.g., LDLR)
Cholesterol Synthesis
(e.g., HMGCR)

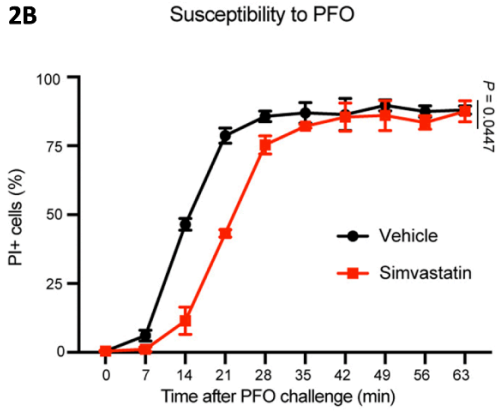
2B
Susceptibility to PFO
PI+ cells (%)
100
75
50
25
0
P = 0.0447
Vehicle
Simvastatin
0
7
14
21
28
35
42
49
56
63
Time after PFO challenge (min)

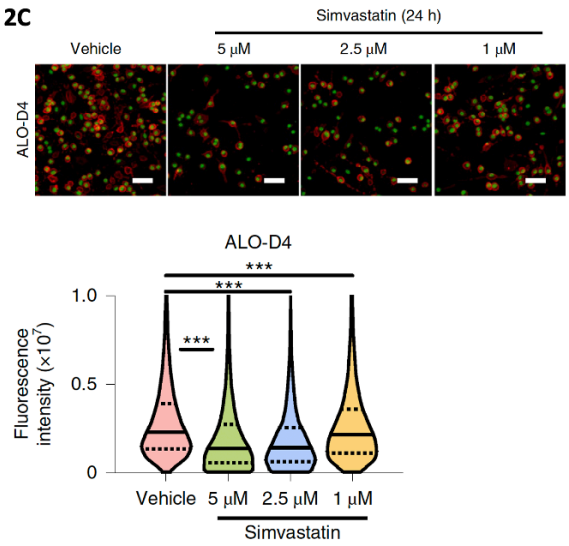
2C
Simvastatin (24 h)
Vehicle
5 μM
2.5 μM
1 μM
ALO-D4
ALO-D4
***
***
***
Fluorescence intensity (x10⁷)
1.0
0.5
0
Vehicle
5 μM
2.5 μM
1 μM
Simvastatin

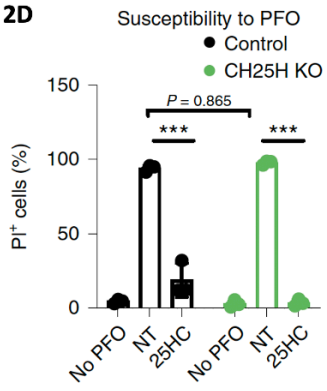
2D
Susceptibility to PFO
Control
CH25H KO
PI+ cells (%)
150
100
50
0
P = 0.865
***
***
No PFO
NT
25HC
No PFO
NT
25HC

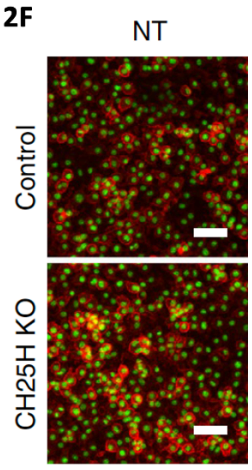
2F
NT
Control
CH25H KO

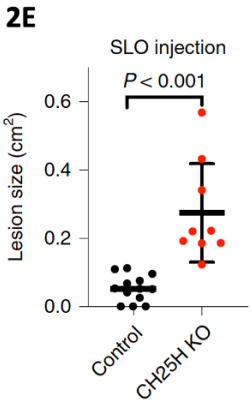
2E
SLO injection
P < 0.001
Lesion size (cm²)
0.6
0.4
0.2
0.0
Control
CH25H KO

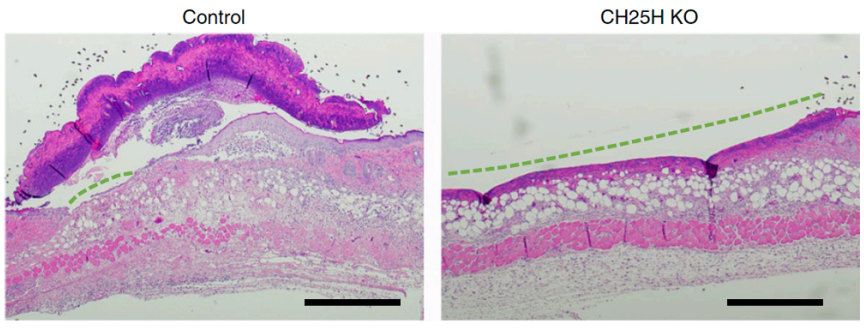
Control
CH25H KO

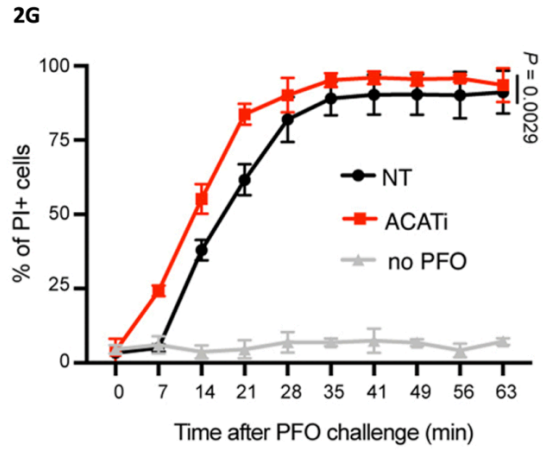
2G
% of PI+ cells
100
75
50
25
0
P = 0.0029
NT
ACATi
no PFO
0 7 14 21 28 35 41 49 56 63
Time after PFO challenge (min)

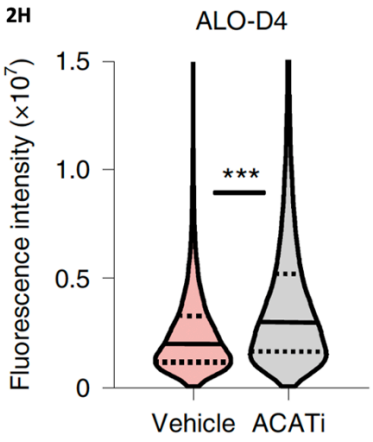
2H
ALO-D4
Fluorescence intensity (×10^7)
1.5
1.0
0.5
0
***
Vehicle
ACATi

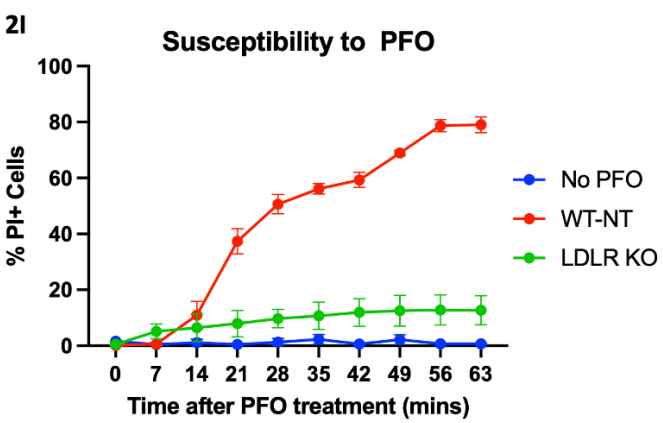
2I
Susceptibility to PFO
% PI+ Cells
100
80
60
40
20
0
No PFO
WT-NT
LDLR KO
0 7 14 21 28 35 42 49 56 63
Time after PFO treatment (mins)

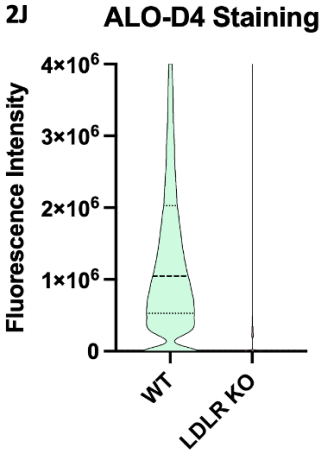
2J
ALO-D4 Staining
Fluorescence Intensity
4×10^6
3×10^6
2×10^6
1×10^6
0
WT
LDLR KO

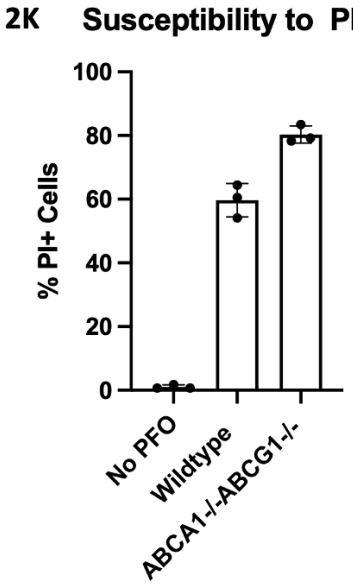
2K
Susceptibility to PFO
% PI+ Cells
100
80
60
40
20
0
No PFO
Wildtype
ABCA1-/-ABCG1-/-

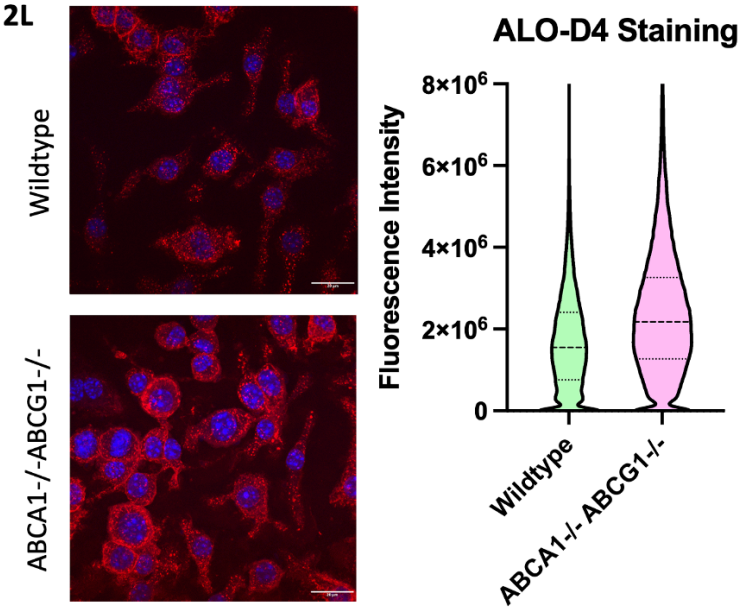
2L
Wildtype
ABCA1-/-ABCG1-/-
ALO-D4 Staining
Fluorescence Intensity
8×10^6
6×10^6
4×10^6
2×10^6
0
Wildtype
ABCA1-/- ABCG1-/-

Chapter 3: Nuclear Receptor Signaling in Relation to CDCs

Nuclear receptors, such as Peroxisome proliferator-activated receptor (PPAR) and Liver X Receptor (LXRs) are lipid-dependent transcription factors that are key regulators of lipid metabolism and inflammation. Many of these nuclear receptor signaling are found to crosstalk with the inflammatory signaling pathways and regulate the innate and adaptive immune system. The ability of these nuclear receptors to integrate metabolic and inflammatory signaling makes them attractive targets for intervention in human metabolic diseases, such as diabetes, and atherosclerosis (*50, 51*).

One of the preliminary observations shown in Chapter 2 is that when BMDMs are activated with LXR agonist, GW3965, cells display robust protection from PFO-mediated cytotoxicity, as well as nearly complete abrogation of ALO-D4 staining (*23*). The manuscript hasn't explored whether interferon signaling directly influences the LXR signaling pathway to monitor host defense. LXR could operate in an independent mechanism, unrelated to the abrogation of cholesterol synthesis and increased cholesterol esterification. This chapter explores some of the initial questions that my thesis project has addressed, in relation to how LXR signaling mediates host defense against CDCs.

Biology of LXRs

As mentioned in Chapter 2, LXR signaling directly opposes the SREBP2 transcriptional axis. Activation of LXR signaling leads to an overall reduction in intracellular cholesterol content through several mechanisms. Primarily, LXR activation leads to increased expression of cholesterol export transporters, ABCA1 and ABCG1, thus increasing cholesterol efflux. Recently, LXR signaling has also been characterized to induce the expression of Inducible degrader of LDLR (IDOL), which leads to the decrease in cholesterol import via polyubiquitination of the LDL receptor (*52*). Furthermore, LXR signaling also leads to an increase in the activity of Aster protein family, which is a nonvesicular-mediated trafficking of

cholesterol between PM and ER (*46*). The combination of these various mechanisms ensure that cells maximize cholesterol removal in response to LXR activation.

Aside from LXR's ability to coordinate cholesterol metabolism, LXR signaling plays an important role in the fatty acid homeostasis in tissues. LXR activation leads to the induction of SREBP1-c, a transcriptional factor that targets genes involved in fatty acid biogenesis (e.g., fatty acid synthase, acetyl-CoA carboxylase, ELOVL fatty acid elongase family) as well as fatty acid desaturation (e.g., stearoyl-CoA desaturase 1 and 2) (*53, 54*). Finally, LXR signaling targets phospholipid remodeling pathways (i.e., the Land's Cycle) via the action of lysophosphatidylcholine acyltransferase 3 (LPCAT3), which will be discussed further in Chapter 4 (*55*).

In addition to modulating lipid homeostasis, LXRs have emerged as important regulators of inflammatory gene expression and innate immunity. Studies have shown that LXRs antagonize inflammatory gene expression downstream of TLR4, IL-1β, and TNF-α mediated signaling. LXR signaling have been shown to use a transcriptional regulatory program known as transrepression. LXRs form obligate heterodimers with the retinoid X-receptor, and the LXR-RXR complex bind to a specific DNA-recognition element, known as LXR-responsive element (LXRE). In the absence of LXR ligands, LXR-RXR complex are believed to be bound to co-repressors, silencing mediator of retinoic acid and thyroid hormone receptor (SMRT) or nuclear receptor corepressor (NCoR). This results in a repression of canonical target gene expression. Upon binding of LXR ligands, a conformational change occurs that causes the release of co-repressors and the recruitment of co-activators, histone acetyltransferase (p300) and activating signal co-integrator 2 (ASC2), resulting in increased transcription of target genes (*56, 57*). Inflammatory genes repressed by LXRs include several NF-κB target genes, such as iNOS, IL-6, MMP9, IL-1β, CCL2, and cyclooxygenase. Conversely, activation of TLR4 inhibits the function of LXRs in cholesterol homeostasis (e.g., reduction of ABCA1) via interferon-regulatory

factor 3, suggesting that LXRs regulate the cross-talk between inflammatory and metabolic pathways (*57*). Aspects of this model remains unclear.

PPARs

Peroxisome-proliferator-activated receptors (PPARs) represent another group of nuclear receptor family that transactivates genes related to lipid metabolism and can also negatively regulate inflammation. The PPAR family is composed of three distinct transcription factors : PPAR-α, PPAR-δ, and PPAR-γ. Each have different tissue specificity, but share overlapping biological functions (*58*). Like LXR's mechanism of action, most PPARs form heterodimers with RXRs, and they're constitutively bound to specific response elements, known as PPAR responsive elements (PPRE), that are present in promoters of target genes (*58*). Ligand-binding initiates a conformational change that results in the degradation of co-repressor complexes, followed by the recruitment of co-activator complexes that subsequently lead to induction of target gene expression. The PPAR family has been shown to modulate various cellular functions, including adipocyte differentiation, fatty-acid oxidation, glucose metabolism, as well as the inhibition of inflammatory gene expression (e.g., NF-κB, NFAT, AP1, and STAT1) (*59, 60*).

LXR and PPARs transactivate similar cassette of genes related to lipid metabolism and inflammation, which led us to ask if PPAR activation in macrophages would manifest similar protection against CDC-mediated cytotoxicity and reduced ALO-D4 binding. However, when macrophages were stimulated with either rosiglitazone (PPAR-γ agonist), cardarine (PPAR-δ agonist), or fenofibrate (PPAR-α agonist), none of the PPAR-activations have shown changes in susceptibility to CDCs nor ALO-D4 binding. Furthermore, rosiglitazone did not protect tissues from CDC-mediated lesion area *in vivo.* Thus, both tissue protection and preserved membrane

integrity are specific to LXR signaling and not a general function of the anti-inflammatory effects of nuclear receptors involved in lipid metabolism.

Acute and local activation of LXR signaling renders skin resistant to toxin-mediated necrosis.

CDCs bind to cholesterol in the membranes of target host cells to induce cytotoxicity. Thus, we reasoned that targeting cholesterol metabolism pharmacologically could provide some measure of protection for tissues challenged with CDCs. The liver X receptors (LXRs) are members of the nuclear receptor superfamily that have a well-defined role in regulating cholesterol homeostasis. LXRs facilitate the removal of excess cholesterol in peripheral tissues by transactivating genes involved in cellular cholesterol efflux, reverse cholesterol transport to the liver, and cholesterol excretion in bile (*53, 56*). To determine if LXR activation would influence the development of ulcerative lesions, we applied LXR agonist GW3965 topically to the skin 24 h before intradermal injection of SLO. As expected, GW3965 robustly induced LXR target genes involved in cholesterol efflux and transport **(Fig. 3A).** Remarkably, skin pre-treatment with GW3965 reduced ulcer lesion area 5-fold in WD-fed mice **(Fig. 3B).** Similar protective effects with GW3965 were observed for chow-fed mice **(Fig. 3B).** Histologic analysis confirmed that GW3965 treatment preserved tissue architecture regardless of diet by limiting injury size, depth, and severity **(Fig 3C, 3D).** Time course studies showed that LXRs could be activated as late as 6 h after SLO injection to reduce ulceration and tissue necrosis **(Fig 3E, 3F).** Importantly, activation of PPARγ, a closely related nuclear receptor involved in regulating fatty acid homeostasis and decreasing inflammation, did not protect tissues from CDC-mediated damage **(Fig. 3G, 3H).** Thus, the tissue protection observed is specific to LXR signaling and not a general function of the anti-inflammatory effects of nuclear hormone receptors involved in lipid metabolism.

LXR-mediated protection from pore-forming toxins does not depend on cholesterol efflux.

One possible mechanism underlying the protective effect of GW3965 from CDCs was the ability of LXRs to promote cellular cholesterol efflux. To test this idea, we used a live cell imaging platform in which cells were cultured in media containing propidium iodide (PI) and challenged with SLO, or PFO to assess cytotoxicity. Productive CDC pore formation and loss of membrane integrity are measured by the percentage of cells that become to PI-positive (PI+) over time. As expected, most cultured macrophages, neutrophils, endothelial cells, and dermal fibroblasts challenged with PFO or SLO become PI+ by the end of the study (60 min or 4 h, respectively), indicating CDC pore-formation and loss of membrane integrity **(Fig. 3I, 3J, 3K, 3L, 3M).** Pretreating cell cultures with GW3965 uniformly and profoundly protected all cell types tested from CDC-mediated loss of membrane integrity and induced LXR target gene expression **(Fig. 3I, 3J, 3K, 3L, 3M).** Importantly, the loss of LXRα and LXRβ (LXR$\alpha\beta^{-/-}$) rendered cells insensitive to GW3965-mediated protection from SLO or PFO **(Fig. 3I, 3J).** Thus, protection is dependent on LXR signaling. ALO-D4 is a modified CDC protein that retains the ability to bind to cholesterol in membranes but has attenuated pore-forming capability. We observed that GW3965 pre-treatment markedly reduced the binding of ALO-D4 to WT macrophages, but not LXR$\alpha\beta^{-/-}$ macrophages, suggesting that LXR activation induces resistance by decreasing CDC recognition of host membranes **(Fig. 3N).** In contrast to the protective effects of LXR signaling, pharmacologic activation of PPARγ with rosiglitazone did not influence CDC-mediated cytotoxicity and ALO-D4 binding for macrophages **(Fig. 3O, 3P).**

The ATP-binding cassette (ABC) transporters ABCA1 and ABCG1 are required for cholesterol efflux from most cells. Thus, we asked if genetic loss of these cholesterol transporters abrogated the LXR-mediated protection from CDCs. We observed that macrophages doubly

deficient in ABCA1 and ABCG1 (A1/G1 DKO) were more sensitive to CDC challenge basally and had increased ALO-D4 binding compared to the control macrophages, consistent with excess cholesterol accumulation in the plasma membrane **(Fig. 3Q, 3R, 3S).** Despite this increased sensitivity to CDC-mediated loss of membrane integrity, we observed that pre-treatment of A1/G1 DKO macrophages with GW3965 markedly reduced the frequency of PI+ positive cells **(Fig. 3Q, 3R)** and decreased ALO-D4 binding to that of control macrophages **(Fig. 3S).** Thus, we conclude that the LXRs can induce protection from CDCs in the absence of ABCA1 and ABCG1-mediated efflux.

LXR-mediated protection from pore-forming toxins does not depend on abrogation of cholesterol synthesis

We also considered the possibility that LXR activation was able to decrease cellular cholesterol content macrophages despite the loss of ABCA1/G1, thereby rendering cells resistant to CDCs. GC-MS analysis of ABCA1/G1 DKO and control macrophages confirmed that loss of these efflux transporters markedly increased the total amounts of cellular cholesterol **(Fig. 3T),** consistent with the heightened sensitivity of ABCA1/G1 DKO macrophages to CDC binding and cytotoxicity. Interestingly, 24 h treatment of macrophages with GW3965 did not decrease total cellular cholesterol amounts in control or ABCA1/G1 DKO macrophages **(Fig. 3T).** We recently showed that interferons (type I and IFNγ) can induce protection to CDCs by decreasing *de novo* cholesterol biosynthesis without influencing total cellular cholesterol amounts. Thus, we asked if LXR agonist decreased *de novo* biosynthesis of cholesterol WT and ABCA1/G1 DKO macrophages. To that end, control and ABCA1/G1 DKO macrophages were treated with GW3965 and cultured with [13]C-glucose for up to 48 h. The synthesized and cholesterol amounts over the 48 h-labeling period were determined using isotopic spectral analysis. ABCA1/G1 DKO macrophages had decreased *de novo* biosynthesis compared to control macrophages, consistent with excess cholesterol accumulation because of diminished

efflux capacity **(Fig. 3U).** GW3965 treatment did not decrease the amounts of synthesized cholesterol accumulated in control or ABCA1/G1 DKO macrophages **(Fig. 3U).** Therefore, the protective effect of LXR signaling on CDC-mediated cytotoxicity could not be attributed to changes in *de novo* synthesis or total cholesterol pool size.

LXR-mediated protection from pore-forming toxins does not depend on cholesterol esterification

It has been shown that heightened cholesterol esterification can decrease the binding of ALO-D4 to cells and protect from CDC cytotoxicity, presumably by moving free cholesterol from membranes into lipid droplet. Thus, we determined if GW3965 treatment of macrophages resulted in cholesterol ester accumulation. However, we observed that 24-48 h treatment of macrophage cultures with GW3965 markedly decreased all species of cholesterol esters measured **(Fig. 3V).** Thus, heightened cholesterol esterification could not account for the robust protection induced by LXR signaling in macrophages. In combination, these data indicate that the pharmacologic activation of LXRs profoundly protect cells and tissues from the harmful effects of CDCs, but this protection occurs independent of changes to cellular cholesterol efflux, biosynthesis, or esterification.

Alternative viewpoint: Microvesicles shedding via LXR

Export of excess cholesterol in macrophages is generally assumed to occur via direct interaction between ABC transporters and high-density lipoproteins (HDLs) or ApoA-1. However, recent observations have addressed that macrophages can actively release cholesterol-containing particles in a form of microvesicles. Thanks to the advancement of scanning electron microscopy and nanoscale secondary ion mass spectrometry (nanoSIMS), one group has found that large numbers of 20- to 120-nm particles are released from the macrophage's filopodia. Interestingly, these macrophage-derived microvesicles have been

shown to be enriched in the metabolically active pool of cholesterol, detected by ALO-D4. The cholesterol content of these microvesicles was increased with cholesterol loading or via stimulation with LXR and RXR agonists (*61*).

It could be possible that LXR activation enables macrophages to secrete these cholesterol-enriched microvesicles as a form of "decoy" against CDCs. We can hypothesize that the most likely reason as to *why* macrophages would secrete these cholesterol-enriched microvesicles is to assist in disposing excess cholesterol, independent of ABC transporters, thus increasing efficiency of cholesterol movement to HDL. However, we could also consider an alternative possibility that an inflammatory stimulus, such as interferons, could potentially cross-talk with LXR signaling (potentially via CH25H-dependent production of 25HC) to coordinate host defense programs. Indeed, interferon stimulation has been shown to induce LXR target genes, such as ABCA1 and ABCG1. As mentioned in the previous chapters, altered cholesterol homeostasis is linked to various inflammatory outcomes, and therefore, it isn't surprising that interferon and LXR signaling operate in the same pathway to combat microbial threats (e.g., Gram-positive bacteria-derived CDCs).

LXR-dependent reshaping of lysophospholipid composition induces resistance to toxin-mediated cytotoxicity.

To identify other LXR-dependent changes to the cellular lipidome that could contribute to CDC protection, we performed shotgun lipidomics on macrophages treated with GW3965, rosiglitazone, or vehicle. We quantitatively measured approximately 800 lipids from 17 subclasses of the macrophage lipidome. Since rosiglitazone treatment did not protect from CDC-mediated tissue necrosis or macrophage cytotoxicity **(Fig. 3W, 3X),** we reasoned the changes to the lipidome induced by both LXR and PPARγ activation were unlikely to be responsible for protection. Thus, we focused on lipids that were changed in response to GW3965 treatment relative to control and rosiglitazone **(Fig. 3W).** Analysis of the lipid subclass

totals revealed that LXR activation decreased lysophosphatidylcholine (LPC), lysophosphatidylethanolamine (LPE), phosphatidylglycerol (PG), Lactosylceramides (LacCER), and cholesterol ester (CE) amounts **(Fig. 3X, 3Y).** No other significant changes in total lipid subclass amounts were observed.

LXR signaling has a well-described role in modulating lysophospholipid (LPL) homeostasis (*53, 55, 62*) by upregulating enzymes involved in transferring fatty acyl chains to the form phospholipids. Indeed, inspection of individual LPCs and LPE species (*e.g.,* LPC 16:0, LPC 18:0, LPC 18:1, LPE 18:0) confirmed that LXR activation specifically decreased the abundance of these lipids **(Fig. 3Z, 3AA).** These data led us to ask if the observed decrease in LPC and LPE might explain LXR's ability to induce protection to CDCs. GW3965 stimulated macrophage were treated with LPC 16:0, LPC 18:0, LPC18:1, LPE18:0 or LPE18:1 followed by SLO challenge. As expected, GW3965 treatment rendered cells refractory to SLO challenge **(Fig. 3AB, 3AC, AD).** Treatment of macrophages with LPC 16:0 or LPC 18:0 alone increased the sensitivity of macrophages to CDC-mediated loss of membrane integrity **(Fig. 3AB, AC, AD),** and increased binding of ALO-D4 to the plasma membrane of macrophages **(Fig. 3AE).** Importantly, the addition of LPC 16:0 or LPC 18:0 was sufficient to abrogate the protective effects of GW3965 **(Fig. 3AB, AC, AD)** from CDC-mediated loss of membrane integrity, and restored ALO-D4 binding to control macrophage levels **(Fig. 3AE).** In contrast, addition of LPE 18:0 or LPE 18:1 to macrophage cultures did not increase sensitivity to CDCs or influence ALO-D4 binding **(3AF, 3AG, 3AH).** Together, these data indicate that LPC levels in host cells play a key role in regulating the binding and pore-formation of CDCs on target cells, and that LXRs can mediate protection to CDCs by reprogramming cellular LPC homeostasis.

LPCs regulate the pool size of "metabolically-active" or "accessible" cholesterol.

Next, we sought to understand the mechanism by which LPCs influenced CDCs -mediated loss of membrane integrity. It has been proposed that CDCs bind to a small but discrete pool of cholesterol in the plasma membrane that is more “accessible” to the toxins than cholesterol tightly associated with sphingomyelin or other phospholipids. This accessible cholesterol pool is in equilibrium with ER-membrane cholesterol and, as such, exerts metabolic influence over the sterol regulatory element binding protein 2 (SREBP2) and the cholesterol metabolic machinery that resides within the ER membrane. These observations led us to ask if pharmacologically expanding the LPC pool would influence the expression of SREBP2-target genes involved in cholesterol biosynthesis and import. Gene expression studies showed that provisioning macrophage cultures with LPC 16:0 decreased expression of *Srebf2*, *Hmgcr*, *Sqle*, and *Ldlr* to approximately 50% that of control cells **(Fig. 3AI),** indicating a decrease in SREBP2 processing and activity. Likewise, [13]C-glucose isotope tracer studies showed supplementation of LPC 16:0 for 24 h decreased *de novo* synthesis of cholesterol without influencing total cellular cholesterol levels **(Fig. 3AJ),** Thus, we conclude that cellular LPC pools regulate the size of the metabolically-active cholesterol pool in the plasma membrane which, in turn, influences ER cholesterol levels and the SREBP-regulated metabolic cholesterol homeostatic program

Methods

***Mouse strains**:* All WT mice were purchased from The Jackson Laboratory: WT C57BL/6 (JAX 000664). LXR$\alpha^{-/-}\beta^{-/-}$ global double knockout, Lys2-cre (JAX 004781) & Vav1-iCre (JAX 008610) Lpcat3 (*LPCAT$^{fl/fl}$)* were kind gifts from Dr. Peter Tontonoz (UCLA), generated as previously described. Lysm-cre ABCA1$^{-/-}$ABCG1$^{-/-}$ mice were a kind gift from Dr. Elizabeth Tarling (UCLA).

***Cells**:* Bone marrow was differentiated into macrophages in DMEM containing 10% v/v FBS (HyClone, GE SH3007103), 5% v/v M-CSF conditioned media, 1% v/v pen/strep, 1% v/v glutamine (Invitrogen) 0.5% v/v sodium pyruvate (Invitrogen) for 7-9 days prior to experimental use. Cells were changed to media with 5% FBS at the time of stimulation. Mouse neutrophils were isolated from bone marrow and purified using EasySep^{TM} Mouse Neutrophil Enrichment Kit (StemCell) and were cultured in RPMI-1640 medium supplemented with 1% v/v pen/strep for up to 6 h. Primary Umbilical Vein Endothelial Cells (HUVEC) were purchased from ATCC (Cat: PCS-100-010) and were cultured in Vascular Cell Basal Medium (Cat: PCS-100-030) supplemented with Endothelial Cell Growth Kit – VEGF (Cat: PCS-100-041). Mouse primary dermal fibroblasts were isolated from skin after digestion of skin with Liberase TM RO (Cat: 5401119001) according to manufacturer's instructions and cultured in DMEM with 10% FBS and 1% v/v pen/strep.

***Extraction of Mouse-Derived Dermal Fibroblasts**:* Fibroblasts were harvested according to Khan M et al. (Generating Primary Fibroblast Culture from mouse ear and tail tissues. Journal of Visualized Experiments. URL: http://www.jove.com/video/53565 DOI: doi:10.3791/53565) Briefly, a piece of skin with 1.5 cm X 1.5 cm was cut and incubated in 70% ethanol for 4 mins and air-dried for 5 mins. The air-dried tissue was minced into smaller pieces (<3 mm pieces) and transferred into 1.8 mL cryotube vials. These minced tissued were placed in collagenase-pronase solution reaching the 1.8 mL mark on the vial, and the vial was shaken horizontally at 200 rpm for 90 mins in 37°C. The digested tissue was placed in a 70 mm cell strainer and grinded with 1 mL

syringe plunger in complete medium (10% FBS, 50 mM 2-mercaptoethanol, 100 mM asparagine, 2 mM glutamine, 1% antibiotic/ mycotic (Gibco 15240062) in RPMI 1640). The cell suspension was spun for 5 mins at 300 g in 4°C and the cell pellet resuspended and cultured in complete medium changing the medium every two days until fibroblast culture was confluent. Cells were used at the first passage. Collagenase solution was prepared by dissolving 10 mg of collagenase D in 4 mL DMEM, and the pronase solution was prepared by dissolving 10 mg of pronase in 10 mM Tris-buffer (pH 8.0) and 1 mM EDTA (pH 8.). Collagenase-pronase solution was made by adding 250 mL of pronase solution to 4 mL of collagenase solution, sterile filtered.

Reagents: Drug agonists: LXR agonist (Selleckchem, GW3965) and PPAR-γ agonist (Sigma, Rosiglitazone). Lipids: 16:0 LysoPC (Avanti, 855675), 18:0 LysoPC (Avanti, 855775), 18:0 LysoPE (Avanti, 856715), and 18:1 LysoPE (Avanti, 846725). PFO is a kind gift from Ajit S. Divakaruni lab (Agilent, 102504-100). Streptolysin O from Streptococcus pyogenes (gamma irradiated, Sigma, S0149-25KU). THY broth (Sigma, T5574-500ML).

Topical Administration of LXR Agonist: WT C57BL/6 mice were shaved on the lower back under isoflurane. DMSO or GW3965 (10 mg/kg of mouse) were topically administered on their lower back and were absorbed by the skin. Equal volumes of DMSO and GW3965 (Approximately 3.5 μL of volume from a 10 mM GW3965 stock solution for female mouse weight of approximately 23 g) were added onto the skin.

Lipidomics Analysis: Macrophages were cultured in 6 well dishes (Fisher, 08-772-1B) and stimulated with DMSO, GW3965, or rosiglitazone. 48 h post-stimulation, cells were imaged for cell count as previously described, scraped and spun down in PBS, and snap-frozen as cell pellets. A modified Bligh and Dyer extraction was carried out on samples. Prior to biphasic extraction, a 13-lipid class Lipidyzer Internal Standard Mix is added to each sample (AB Sciex, 5040156). Following two successive extractions, pooled organic layers were dried down in a Genevac EZ-2

Elite. Lipid samples were resuspended in 1:1 methanol/dichloromethane with 10 mM Ammonium Acetate and transferred to robovials (ThermoFisher, 10800107) for analysis. Samples were analyzed on the Sciex Lipidyzer Platform for targeted quantitative measurement of 1100 lipid species across 13 classes. Differential Mobility Device on Lipidyzer was tuned with SelexION tuning kit (Sciex, 5040141). Instrument settings, tuning settings, and MRM list available upon request. Data analysis was performed according to the workflow published by Su, B. et al.

***Isotope Enrichment Experiments*:** All isotope labeling experiments from BMDMs were performed as previously described. In brief, day 8 differentiated BMDMs were transferred to complete media containing 50% [13C]-glucose (Cambridge Isotope Laboratories, CLM-1396-MPT-PK) with DMSO or GW3965 for 48 h before collection. Analysis of labeled fatty acids and cholesterol was performed as described previously. The relative contributions of synthesis to the total cholesterol pool over the 48 h-labeling period were determined by fitting the isotopologue distributions for cholesterol in a model similar to Isotopomer Spectral Analysis (ISA) as described previously.

***In vivo SLO injection*:** All *in vivo* SLO injections were performed as previously describe. SLO was activated with 10 mM DTT at room temperature. 72 h later, photographs of the skin lesions were taken, and the lesion area (in cm^2) was measured using the ImageJ software. Wild type C57/BL6 mice fed on either chow or WD were shaved on the lower back and were either topically pre-treated with LXR agonist, GW3965 (10 mg/kg of mouse) for 24 h, or topically treated post-SLO injection (8 kU/mouse) at different time points. Lesion sizes were quantified as above 72 hours after injection. Tissue samples were collected for histological analysis in UCLA Translational and Pathology Core Laboratory, as well as for RNA preparation in RNAlater™ Stabilizing Solution (ThermoFischer, Catalog No. AM7020).

RNA Extraction from skin tissues: Tissues were minced into smaller pieces in homogenizer tubes containing ceramic beads (Omni, SKU 19-646). 1 mL of Trizol (ThermoFisher, 15596-018) was added to each sample, and the tissues were homogenized using Omni Tissue Homogenizer (Omni, SKU 19-042E) at 3 cycles of 0.23 meters per second. The homogenized tubes were spun down for 10 minutes and the Trizol supernatant was transferred to another 1.5 mL tube for subsequent RNA extraction procedures using manufacturer's protocol.

Gene expression analysis: RNA was extracted from all cells with Trizol (ThermoFisher, 15596-018) using manufacturer's protocols. cDNA was synthesized with high-capacity cDNA reverse transcription kit (Applied Biosystems, 4368814) as per manufacturer's instructions (700 ng/μL RNA per cDNA synthesis reaction). Quantitative PCR (qPCR) was conducted on the Roche LightCycler 480 using SYBR Green Master Mix (Kapa Biosciences) or PowerUp™ SYBR™ Green Master Mix (ThermoFisher, A25778) and 0.5 μmol/L primers. Relative expression values are normalized to control gene (*36b4*) and expressed in terms of linear relative mRNA values. A list of qPCR primers are available upon request.

CDC Permeabilization Live Imaging: All *in vitro* CDC cytotoxicity assay were performed as previously described. BMDMs, neutrophils, HUVECs, and dermal fibroblasts were seeded 50 k/well on 96 well plates (E&K Scientific, EK-25090, Greiner). Cells were left for 2 days before stimulation with GW3965 or rosiglitazone for 24 h. Culture media were replaced by 37 ˚C PBS with 0.05% BSA, 1 μg/mL propidium iodide (PI) (VWR, 80057-368) and 5 μg/mL Hoechst 33342 (ThermoFisher, H3570). Then cells were challenged by spiking recombinant PFO (final concentration 1 nM) or gamma-irradiated SLO (final concentration 22 nM), and plates were imaged every 7 min on Molecular Devices ImageXpress XL using a 20x Objective (Nikon Plan Fluor, 0.3 NA). SLO was activated with the addition of 10 mM DTT in room temperature for 15 minutes. Total (Hoechst 33342-positive) and permeabilized (PI-positive) cell number were

assessed using MetaXpress Software with Powercore using the Multi-wavelength cell scoring module.

Purification of ALO-D4, Conjugation of Fluorophore onto ALO-D4, and Binding of ALO-D4 onto Cells: These studies were performed as described previously. Briefly, ALO-D4 protein was purified using standard histidine-tagged affinity chromatography and concentrated into 1 mg/mL. Purified protein was conjugated with Alexa-594 and stored at 4˚C. Cells were seeded 100k/well and stimulated with DMSO, GW3965, or rosiglitazone for 24h. After stimulation, cells were incubated with ALO-D4, as described previously. Unbound proteins were removed by washing with PBS/Ca^{2+}/Mg^{2+} three times for 2 min each.

Quantification of Fluorescence Intensity: Fluorescent images were taken at UCLA Molecular Screening Shared Resource core facility on a Molecular Device ImageXpress Confocal using a 20x Objective (Nikon Plan Fluor, 0.3 NA). on a Molecular Devices ImageXpress XL. Maximum projected cellular fluorescence intensity was assessed by MetaXpress Software with Powercore using the Multi-wavelength cell scoring module, as described previously.

Histology: Skin was fixed overnight in 10% neutral buffered formalin followed by standard histologic processing. H&E stained slides were evaluated by a board certified dermatopathologist. Histologic ulceration scores were determined according to the following scale: 0 – no ulceration/ erosion (only dermal inflammation and edema, 1- erosion, 2- erosion/ulceration, 3- epidermal ulceration, 4 – epidermal and dermal ulceration, 5 – full thickness ulceration of epidermis, dermis, and panniculus.

Figure Legends

Fig 3 || (A) qPCR of genes from skin tissue treated with topical DMSO or GW3965 (10 mg/kg) for 24h. **(B, C, D)** Quantification of lesion area, representative photomicrographs of histology, and histologic ulceration scoring from mice fed chow or WD for 8 weeks and then treated topically with LXR agonist GW3965 (10 mg/kg) or DMSO 24h prior to SLO injection. Yellow dashed line= erosion, gray dashed line=ulceration. Scale=500μm. **(E)** Representative lesion images from mice topically treated with topical GW3965 (10 mg/kg) concurrently with intradermal SLO injection (8 kU/mouse), or the indicted time after SLO injection. Lesions are marked with white arrow. **(F)** Quantification of lesion area from mice topically treated with GW3965 (10 mg/kg) concurrently with intradermal SLO injection or indicted time after SLO injection. **(G)** Quantification of SLO-induced lesion size from skin of mice treated with topical with either DMSO or rosiglitazone (10 mg/kg) 24h before intradermal SLO injection. **(H)** qPCR for PPAR-γ target genes from skin treated with DMSO or rosiglitazone (10 mg/kg) 24h. **(I, J)** Percentage of propidium iodide-positive (PI+) WT and LXR $\alpha^{-/-}\beta^{-/-}$ bone marrow-derived macrophages (BMDMs) in cultures treated with LXR agonist GW3965 (1 μM) or DMSO for 24h, and then challenged with streptolysin-O (SLO) for 4h in media containing PI. **(K, L, M)** Percent PI+ bone marrow derived neutrophils, human umbilical vein endothelial cells (HUVEC), or mouse dermal fibroblasts stimulated with either DMSO or GW3965 (1 μM) for 6 h, 24h, and 24h, respectively, and then challenged with PFO for 60 mins in media containing PI. Cells were imaged every 7 minutes to assess changes in PI influx. **(N)** Representative confocal images of WT and LXR $\alpha^{-/-}\beta^{-/-}$ BMDMs cultures treated with GW3965 (1 μM) or DMSO for 24h and then stained with fluorescent ALO-D4 and DAPI. Violin plots of cellular fluorescent intensity (from left to right: n = 19,375 18,841 20,263 and 17,641 cells measured). **(O)** Confocal images of WT BMDMs stimulated with rosiglitazone (1 μM) for 24 h and then stained with fluorescent ALO-D4 and DAPI, as well as corresponding violin plots of cellular fluorescent intensity. **(P)** Percent PI+

WT BMDMs treated with DMSO or PPAR-γ agonist rosiglitazone (1 μM) for 24h and then challenged with SLO (4h), as above. **(Q, R)** Percent PI+ WT or ABCA1$^{-/-}$ABCG1$^{-/-}$ BMDMs treated with DMSO or GW3965 as above and then challenged with SLO (4h) in media containing PI. **(S)** ALO-D4 staining of WT and ABCA1$^{-/-}$ABCG1$^{-/-}$ BMDMs stimulated with GW3965 (1 μM) for 24h. Violin plots of cellular fluorescent intensity (from left to right: n = 23,152 18,435 19,535 and 21,056 cells measured). **(T, U)** Total and net synthesized cholesterol (nmol/10^7 cells) from WT and ABCA1$^{-/-}$ABCG1$^{-/-}$ BMDMs treated with DMSO or GW3965 (1 μM) for 48h. Total and synthesized cholesterol was measured by GC-MS using isotopologue spectral analysis (ISA) modeling. **(V)** Total cholesterol ester (CEs; nmol/10^7 cells) from BMDMs stimulated with DMSO, GW3965 (1 μM), or rosiglitazone (1 μM) for 48 h. CE pool sizes were determined by direct infusion MS. Data are representative of three independent experiments. **(W)** Heatmap showing total lipid composition in WT BMDMs stimulated with either DMSO, GW3965 (1 μM), or rosiglitazone (1 μM) for 48 h. **(X)** Total lysophosphatidylcholine (LPC) species (nmol/10^7 cells) of BMDMs treated with DMSO, GW3965 (1 μM), or rosiglitazone (1 μM) for 48h. Quantification of lysophospholipids were determined by direct infusion MS. **(Y)** Total lysophosphatidylethnanolamine (LPE), phosphatidylglycerol (PG), and lactosylceramide (LacCER) species (nmol/10^7 cells) of BMDMs treated with DMSO, GW3965 (1 μM), or rosiglitazone (1 μM) for 48h. Quantification of lysophospholipids were determined by direct infusion MS. **(Z)** Quantification of individual LPC species (LPC 16:0, 16:1 and 18:1) of BMDMs treated with DMSO, GW3965 (1 μM), or rosiglitazone (1 μM) for 48h. **(AA)** Quantification of individual LPE species (LPE 18:0 and 18:1) of BMDMs treated with DMSO, GW3965 (1 μM), or rosiglitazone (1 μM) for 48h. **(AB, AC, AD)** Percent PI+ WT BMDMs treated with vehicle, GW3965 (1 μM), LPC 16:0 (20 nM), LPC 18:0 (20 nM) alone or in combination for 24h and then challenged with SLO (4h) in media containing PI. **(AE)** Confocal images of WT BMDMs stimulated with DMSO, GW3965 (1 μM), LPC 16:0 (20 nM) alone or LPC 16:0 (20 nM) and GW3965 in combination for 24h and then stained with fluorescent ALO-D4 and DAPI. Violin

plots of cellular fluorescent intensity (from left to right: n= 12,573 10,572 18,118 and 16,704). **(AF)** Percentage PI+ WT BMDMs treated with vehicle, LPE 18:0 (20 nM) or LPE 18:1 (20 nM), and then challenged with SLO (4h) in media containing PI. **(AG)** Confocal images of WT BMDMs stimulated with vehicle or LPE 18:0 and then stained with fluorescent ALO-D4 and DAPI. Violin plots of cellular fluorescent intensity (from left to right: n= 8,535 and 9,621). **(AH)** Confocal images of WT BMDMs stimulated with vehicle or LPE 18:1 and then stained with fluorescent ALO-D4 and DAPI. Violin plots of cellular fluorescent intensity (from left to right: n= 9,031 and 9,159). **(AI)** Expression of cholesterol metabolism genes from BMDMs treated with vehicle or LPC 16:0 (20 nM) for 24h. **(AJ)** Total and net synthesized cholesterol (nmol/10^7 cells) from WT BMDMs treated with vehicle or LPC 16:0 (20 nM) for 48h. Total and synthesized cholesterol was measured by GC-MS using ISA modeling.

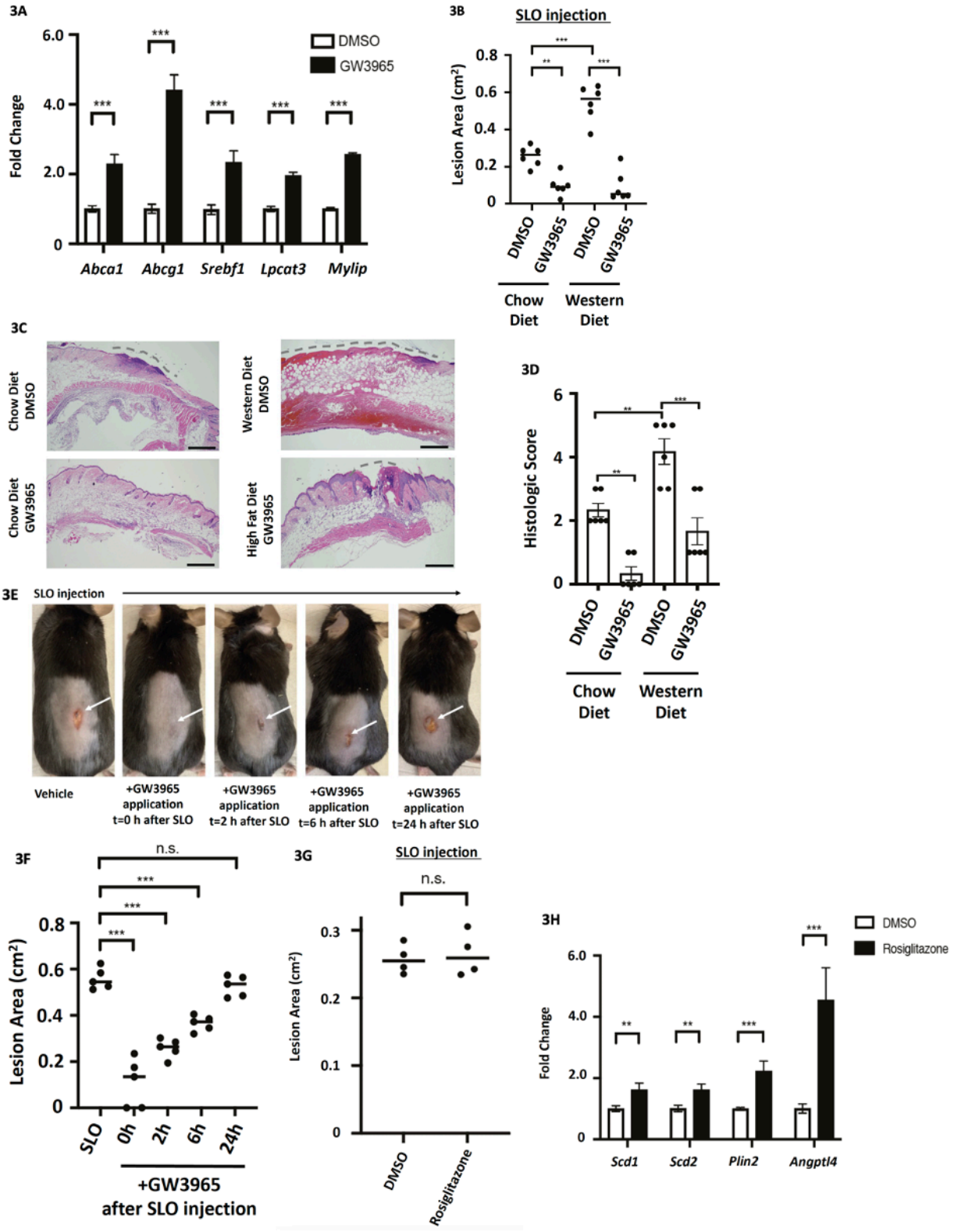
3A
Fold Change
DMSO
GW3965
Abca1
Abcg1
Srebf1
Lpcat3
Mylip
3B
SLO injection
Lesion Area (cm²)
DMSO
GW3965
Chow Diet
Western Diet
3C
Chow Diet DMSO
Western Diet DMSO
Chow Diet GW3965
High Fat Diet GW3965
3D
Histologic Score
3E
SLO injection
Vehicle
+GW3965 application t=0 h after SLO
+GW3965 application t=2 h after SLO
+GW3965 application t=6 h after SLO
+GW3965 application t=24 h after SLO
3F
n.s.
Lesion Area (cm²)
SLO
0h
2h
6h
24h
+GW3965 after SLO injection
3G
SLO injection
n.s.
Lesion Area (cm²)
DMSO
Rosiglitazone
3H
DMSO
Rosiglitazone
Fold Change
Scd1
Scd2
Plin2
Angptl4

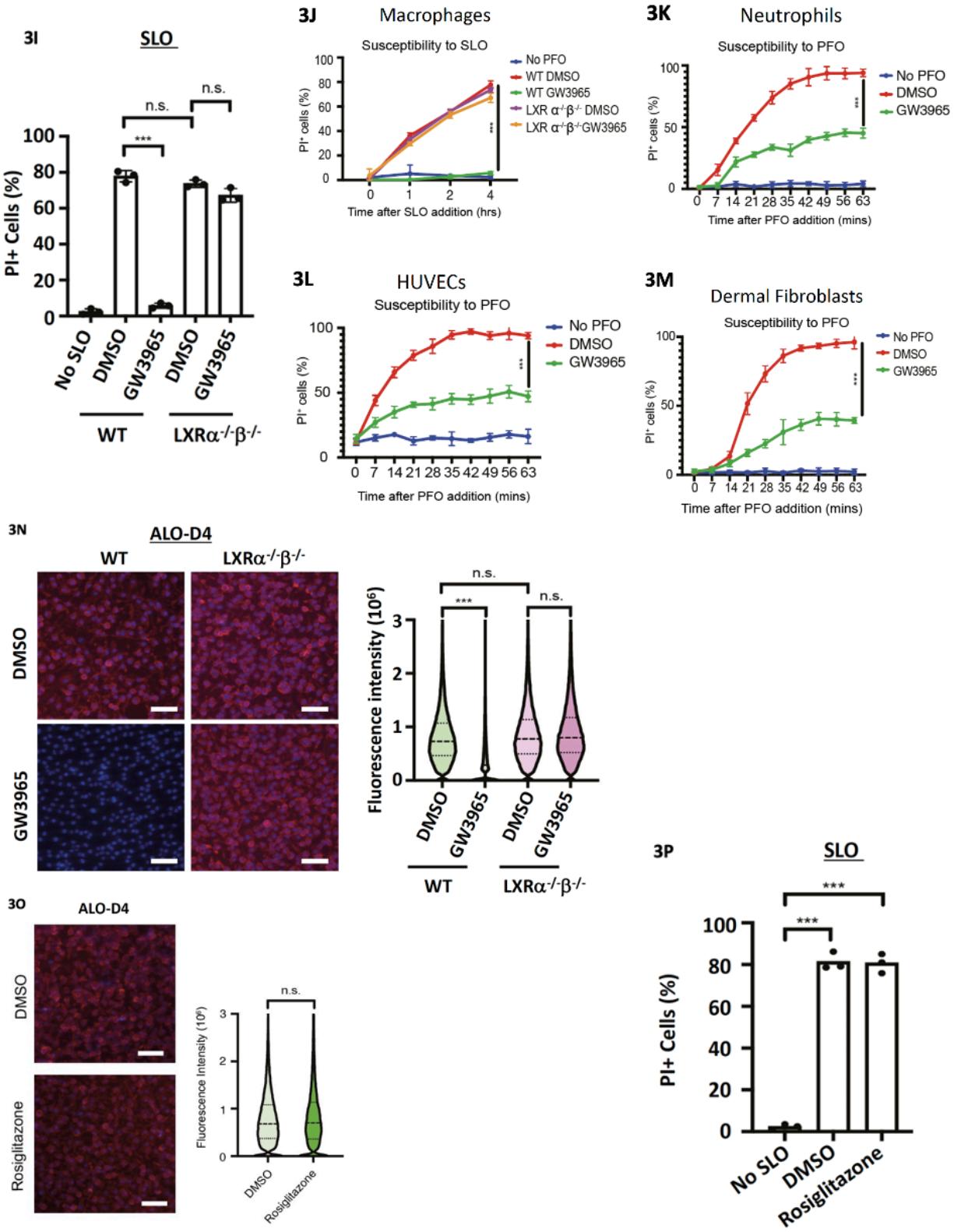
3I
SLO
PI+ Cells (%)
n.s.
n.s.
***
No SLO
DMSO
GW3965
DMSO
GW3965
WT
LXRα-/-β-/-
3J
Macrophages
Susceptibility to SLO
PI+ cells (%)
No PFO
WT DMSO
WT GW3965
LXR α-/-β-/- DMSO
LXR α-/-β-/-GW3965
Time after SLO addition (hrs)
3K
Neutrophils
Susceptibility to PFO
PI+ cells (%)
No PFO
DMSO
GW3965
Time after PFO addition (mins)
3L
HUVECs
Susceptibility to PFO
PI+ cells (%)
No PFO
DMSO
GW3965
Time after PFO addition (mins)
3M
Dermal Fibroblasts
Susceptibility to PFO
PI+ cells (%)
No PFO
DMSO
GW3965
Time after PFO addition (mins)
3N
ALO-D4
WT
LXRα-/-β-/-
DMSO
GW3965
Fluorescence intensity (10⁶)
n.s.
***
n.s.
DMSO
GW3965
DMSO
GW3965
WT
LXRα-/-β-/-
3O
ALO-D4
DMSO
Rosiglitazone
Fluorescence Intensity (10⁶)
n.s.
DMSO
Rosiglitazone
3P
SLO
PI+ Cells (%)
***
***
No SLO
DMSO
Rosiglitazone

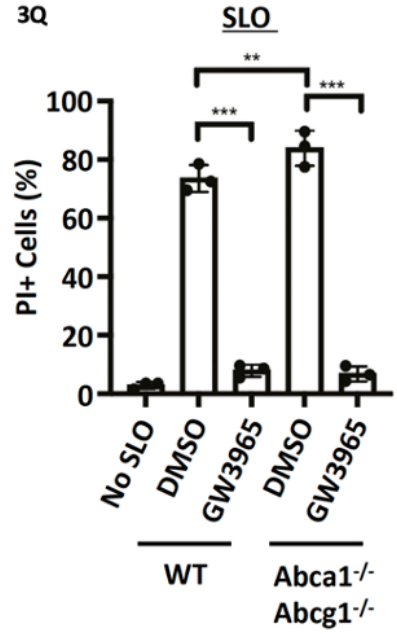
3Q
SLO
PI+ Cells (%)
100
80
60
40
20
0
**
***
***
No SLO
DMSO
GW3965
DMSO
GW3965
WT
Abca1-/-
Abcg1-/-

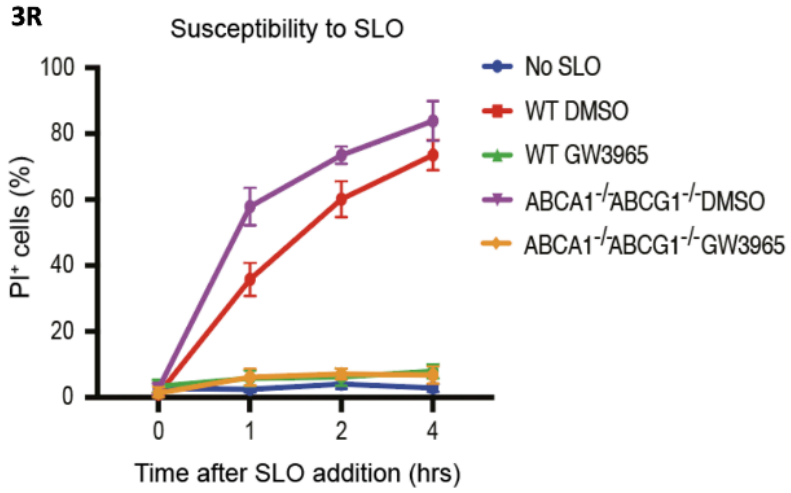
3R
Susceptibility to SLO
PI+ cells (%)
100
80
60
40
20
0
0
1
2
4
Time after SLO addition (hrs)
No SLO
WT DMSO
WT GW3965
ABCA1-/-ABCG1-/-DMSO
ABCA1-/-ABCG1-/-GW3965

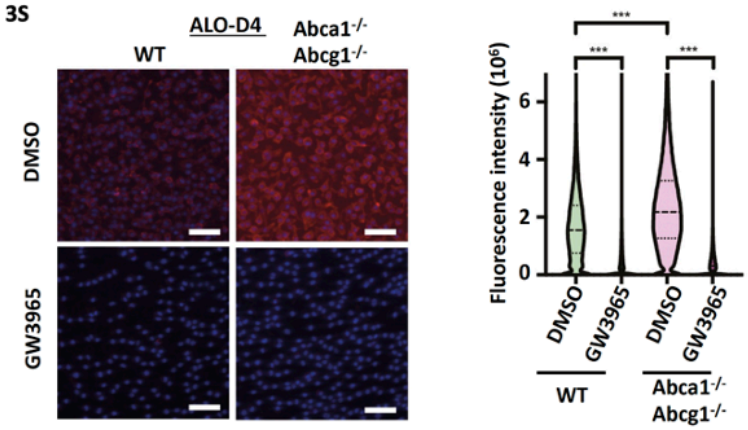
3S
ALO-D4
WT
Abca1-/-
Abcg1-/-
DMSO
GW3965
Fluorescence intensity (10⁶)
6
4
2
0
***
***
***
DMSO
GW3965
DMSO
GW3965
WT
Abca1-/-
Abcg1-/-

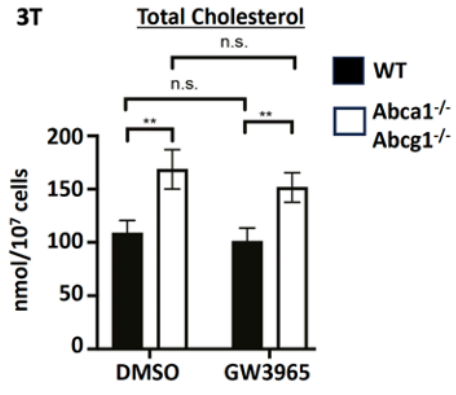
3T
Total Cholesterol
nmol/10⁷ cells
200
150
100
50
0
n.s.
n.s.
**
**
WT
Abca1-/-
Abcg1-/-
DMSO
GW3965

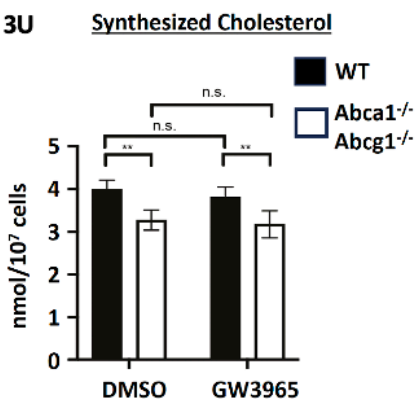
3U
Synthesized Cholesterol
nmol/10⁷ cells
5
4
3
2
1
0
n.s.
n.s.
**
**
WT
Abca1-/-
Abcg1-/-
DMSO
GW3965

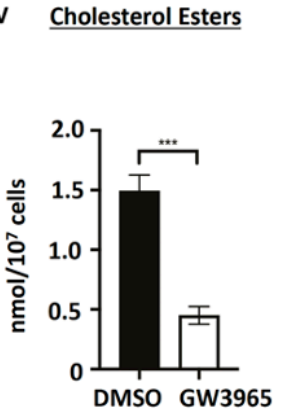
3V
Cholesterol Esters
nmol/10⁷ cells
2.0
1.5
1.0
0.5
0
***
DMSO
GW3965

3W

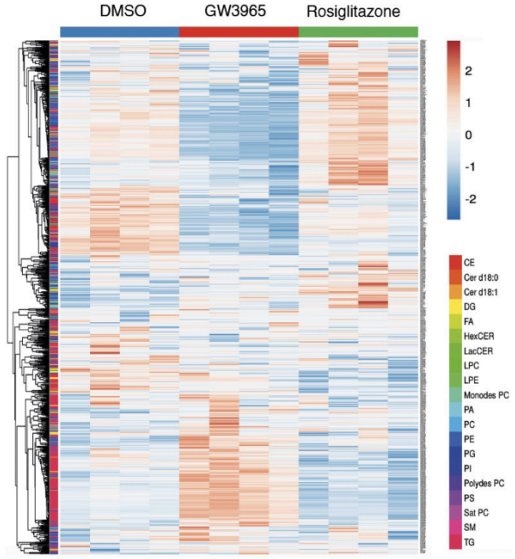

3X

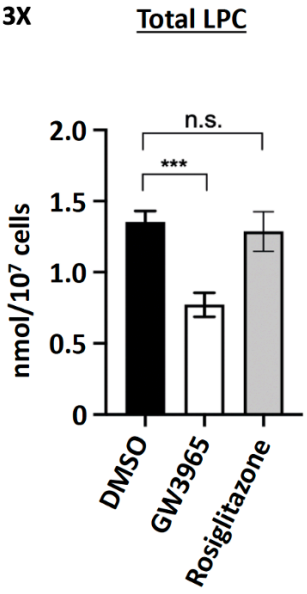

3Y

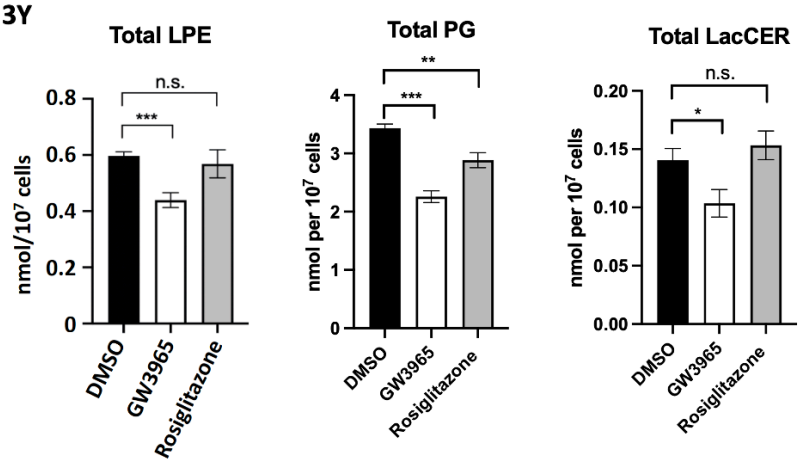

3Z

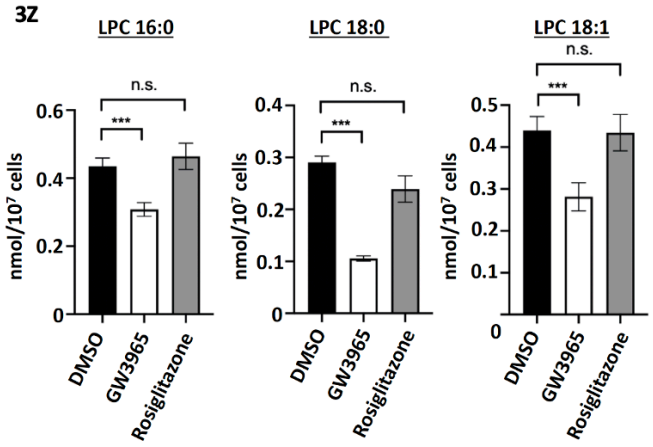

3AA

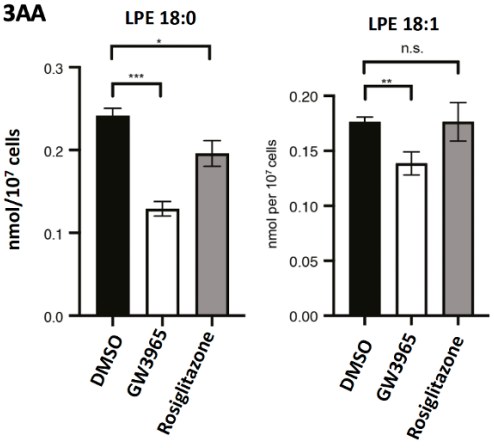

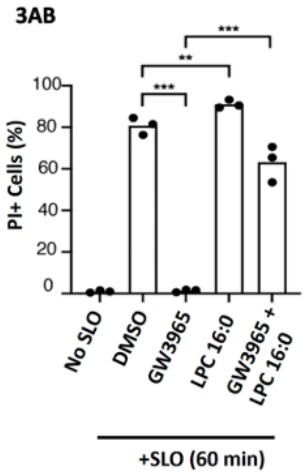
3AB
PI+ Cells (%)
No SLO
DMSO
GW3965
LPC 16:0
GW3965 + LPC 16:0
+SLO (60 min)

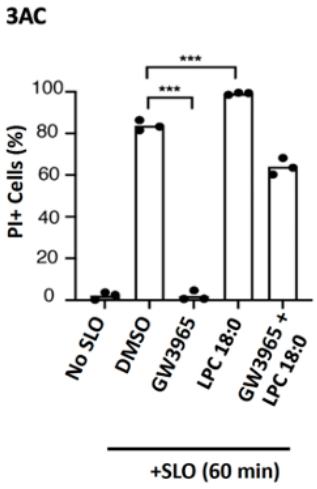
3AC
PI+ Cells (%)
No SLO
DMSO
GW3965
LPC 18:0
GW3965 + LPC 18:0
+SLO (60 min)

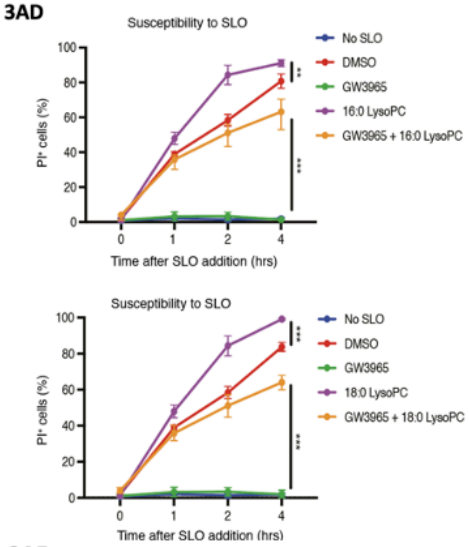
3AD
Susceptibility to SLO
PI+ cells (%)
Time after SLO addition (hrs)
No SLO
DMSO
GW3965
16:0 LysoPC
GW3965 + 16:0 LysoPC
Susceptibility to SLO
PI+ cells (%)
Time after SLO addition (hrs)
No SLO
DMSO
GW3965
18:0 LysoPC
GW3965 + 18:0 LysoPC

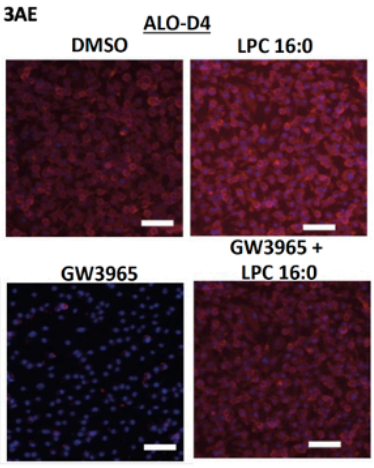
3AE
ALO-D4
DMSO
LPC 16:0
GW3965
GW3965 + LPC 16:0

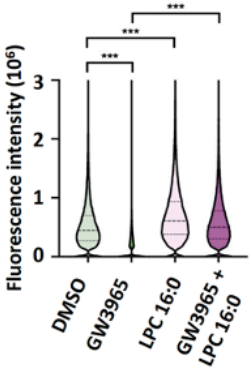
Fluorescence intensity (10⁶)
DMSO
GW3965
LPC 16:0
GW3965 + LPC 16:0

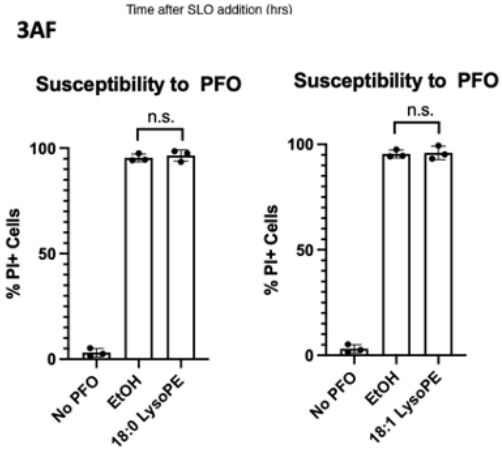
3AF
Susceptibility to PFO
% PI+ Cells
n.s.
No PFO
EtOH
18:0 LysoPE
Susceptibility to PFO
% PI+ Cells
n.s.
No PFO
EtOH
18:1 LysoPE

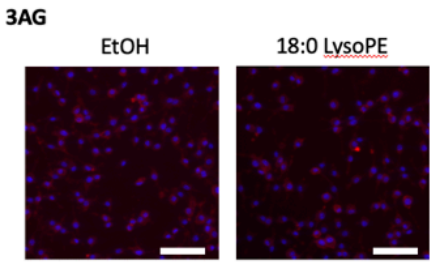
3AG
EtOH
18:0 LysoPE

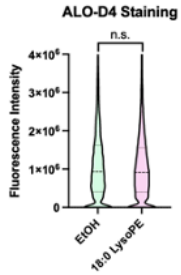
ALO-D4 Staining
n.s.
Fluorescence Intensity
EtOH
18:0 LysoPE

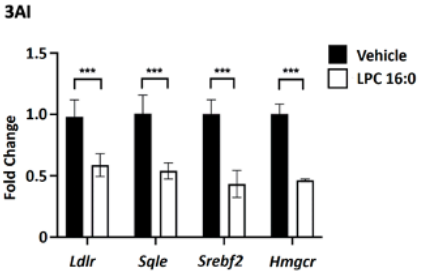
3AI
Vehicle
LPC 16:0
Fold Change
Ldlr
Sqle
Srebf2
Hmgcr

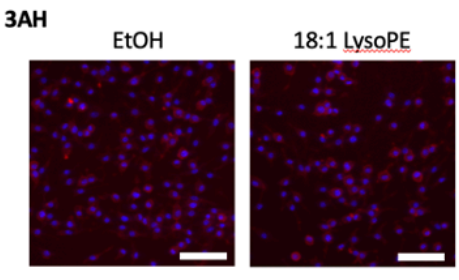
3AH
EtOH
18:1 LysoPE

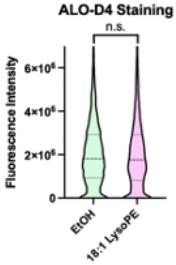
ALO-D4 Staining
n.s.
Fluorescence Intensity
EtOH
18:1 LysoPE

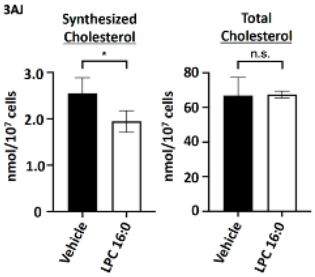
3AJ
Synthesized Cholesterol
nmol/10⁷ cells
Vehicle
LPC 16:0
Total Cholesterol
nmol/10⁷ cells
Vehicle
LPC 16:0

Chapter 4: Phospholipid Metabolism in Relation to CDCs and Group A Strep

Background on Phospholipids

Phospholipids (PLs) play a major role in the foundation of all living organisms, both prokaryotes and eukaryotes. They are the most abundant lipids in the plasma membrane. At the basic level, PLs have a phosphate-containing hydrophilic head group, a glycerol backbone, and non-polar hydrophobic fatty acid (FA) chains (*63*). The *sn-1* and *sn-2* positions of the glycerol backbone are esterified with fatty acids of varying length and degree of saturation (*64*). The remaining *sn-3* is esterified with phosphoric acid, which is in turn esterified with short-chain alcohol of varying chemical structure forming the hydrophilic head group. Different functional groups are attached to the phosphate heads. Amongst the most common are phosphatidylcholine (PC), phosphatidylethanolamine (PE), phosphatidylserine (PS), phosphatidylinositol (PI), and phosphatic acid (PA). For example, PC 16:0_18:2 refers to a phosphatidylcholine consisting of two fatty acids: 16-carbon FA with all single bonds and 18-carbon FA with two double bonds. Each of these PL classes can mediate diverse functions (*64*). While the majority of the phospholipids play an integral role in the lipid bilayer to ensure barrier function and biophysical/biochemical characteristics, they may also be involved in specialized signaling functions. For example, during apoptosis or platelet activation, PS lipids tend to flip across from the inner leaflet to the outer leaflet, effectively creating an “eat me” signal on dead cells or a scaffold for blood-clotting factors on activated platelets (*65*). PI serves as an important phospholipid in the context of PI3K-Akt signaling (*66, 67*).

Thanks to the recent advancements in shotgun lipidomics, researchers can profile and quantify PL fatty acyl compositions of biological membranes. Most eukaryotic plasma membrane is highly enriched in PC (over 50% of the PLs), and many PLs are found associated with other types of lipids, such as cholesterol and sphingomyelin (*64*). Given the breadth of PL diversity and function, it is unsurprising that alterations in PL composition beyond homeostasis lead to pathological conditions and diseases. Phospholipids containing oxidized fatty acid residues (OxPLs) were shown to induce pro-inflammatory changes in endothelial cells. OxPLs

were characterized as the major component of minimally oxidized low-density lipoprotein responsible for its ability to induce synthesis of inflammatory cytokines and chemokines, as well as stimulation of adhesion of monocytes to endothelial cells (ECs) (*68, 69*). Furthermore, another study has shown that PC supplementation for 35 days has prevented inflammatory responses and behavioral disturbances in LPS-induced mice. This occurs via amelioration of gut barrier damage and improved microbiome health via modulating cell adhesion molecule (CAM) pathways, as well as increased production of short-chain fatty acid (*70, 71*).

Phospholipid Metabolism

Phospholipid metabolism is a very intricate and tightly regulated pathway in mammalian cells. Early studies by Eugene Kennedy in the late 1950s and early 1960s focused on the synthesis of PC and PE. Now known as the Kennedy pathway, it involves three enzymatic reactions: phosphorylation of choline by choline kinase, formation of CDP-choline from phosphocholine and CTP via CTP:phosphocholine cytidyltransferase, and the replacement of cytidine monophosphate by diacylglycerol (DAG) to synthesize PC via CDP-choline: 1,2-diacylglycerol cholinephosphotransferase. A similar mechanism occurs for synthesis of PE, except that the precursor molecule is ethanolamine. DAG is synthesized from PA, which makes PA a central metabolite in the synthesis of all phospholipid species that are catalyzed via CPD-DAG exchange (*72, 73*).

As mentioned above, the fatty acyl chains in phospholipids are highly diverse and asymmetrically distributed. This distribution cannot be fully explained by the Kennedy Pathway because the enzymes in this *de novo* biosynthesis pathway have little specificity to fatty acyl-CoA. In 1958, William EM Lands has characterized an alternate pathway that involves remodeling of phospholipids. He and colleagues proposed that membrane phospholipids are metabolically active and undergo a series of deacylation and reacylation reactions, which results in the removal and reattachment of polyunsaturated fatty acyl CoAs at the *sn-2* position (*74, 75*).

Upon *de novo* synthesis, the fatty acyl chains at the *sn-2* position are hydrolyzed via phospholipase A2 (PLA2) to generate lysophospholipids (lysoPL). These lysoPLs are subsequently re-acylated by LPLATs to incorporate another fatty acid to the same *sn-2* position to form a new PL species.

Lysophosphatidylcholine Acyltransferase (LPCAT)

LPCAT is a type of LPLATs that primarily plays a role in remodeling PC and lysoPC homeostasis (*76*). Other LPLAT proteins are implicated in the remodeling pathway between other types of LysoPLs and PLs (e.g., LPEAT, LPIAT, LPSAT, etc.). LPCAT is composed of four family proteins: LPCAT1, LPCAT2, LPCAT3, and LPCAT4.

LPCATs have distinct tissue distributions, enzymatic activities, and substrate preferences. LPCAT1 is primarily expressed in lung alveolar type II cells, spleen, and the brain. Its substrate specificity include 16:0-CoA, 18:2-CoA, and 18:3-CoA (*77*). LPCAT2 is highly expressed in inflammatory cells (e.g., macrophages and neutrophils), skin, colon, and the brain. It is highly specific for 20:4-CoA (*78*). LPCAT3 is more universally expressed, but it is most abundant in testis, kidney, macrophages, and metabolic tissues such as liver, intestine, and adipose. Interestingly, LPCAT3 has an enzymatic activity as LysoPE and LysoPS acyltransferase, in addition to LysoPC acyltransferase, thus producing the products PE, PS, and PC. LPCAT3 has high substrate specificity for 18:2-CoA and 20:4-CoA. LPCAT4 is selectively expressed in epididymis, brain, testis, and ovary (*69, 79*). Like LPCAT3, LPCAT4 has an enzymatic function as LysoPE acyltransferase, and it has substrate specificity for 18:1-CoA and 18:2-CoA.

Disruption of LPCAT3 increases the metabolically-active cholesterol pool and reprograms SREBP2-dependent cholesterol homeostasis

We next used a loss-of-function genetic model to test the hypothesis that dysregulation of LPC homeostasis influences metabolically-active cholesterol. Shotgun lipidomics confirmed that *Lpcat3*-deficient macrophages accumulated LPC 16:0 and LPC 18:0, and were deficient in select PC species containing arachidonic acid or other PUFA acyl tails (*e.g.,* PC 16:0_18:2, 16:0_20:4) **(Fig. 4A, 4B).** Gene expression studies revealed that quiescent *Lpcat3*-deficient macrophages had decreased expression of SREBP2 target genes *Hmgcr*, *Sqle* and *Ldlr*, consistent with reduced SREBP2 activity **(Fig. 4C).** [13]C-glucose isotope tracer studies confirmed that *Lpcat3*-deficent macrophages synthesize less cholesterol than their control counterparts and had decreased total cholesterol **(Fig. 4D).** Thus, disruption of LPCAT3 phenocopies pharmacologic addition of LPCs, and influences the SREBP2-mediated cholesterol homeostatic program in the ER. These data further support the idea that LPC homeostasis influences cellular cholesterol metabolism through modulation of the metabolically-active cholesterol pool.

Loss of LPCAT3 increases sensitivity to CDCs and increased metabolically-active pool

We asked if the increased accessible cholesterol observed in *Lpcat3*-deficient macrophages translated into heightened sensitivity to CDCs. Quiescent control and *Lpcat3*-deficient macrophages were challenged with PFO or SLO (as above in Fig. 2), and PI+ cell frequency was measured over time. Strikingly, there was a left shift in the kinetics of Lpcat3-deficient cells becoming PI+ and a greater percentage of the Lpcat3-deficient cells becoming positive by the end of the challenge **(Fig. 4E, 4F).** We also observed increased ALO-D4 binding to quiescent *Lpcat3*-deficient macrophages **(Fig. 4G).** Together, these data suggest that loss of LPCAT3, and the accompanying increase in accessible or metabolically-active cholesterol, influences CDC binding and resultant susceptibility to CDC-dependent pore formation. We also asked if the loss of LPCAT3 maximally filled the metabolically accessible pool, or if this pool could be further increased. Sphingomyelinase treatment has been previously shown to rapidly increases

the metabolically active/accessible cholesterol pool. We found that a brief 20 min sphingomyelinase treatment of *Lpcat3*-deficient macrophages further enhanced ALO-D4 binding **(Fig. 4H).** These data indicate that increasing LPCs amounts in the membrane does not maximally fill the accessible or metabolically-active pool, and further supports the idea that LPC homeostasis can be a physiologic regulator of this critical cholesterol pool.

Loss of LPCAT3 increases tissue sensitivity *in vivo*

Next, we determined if selective LPCAT3 deficiency in endothelial and immune cells renders mice more susceptible to SLO *in vivo*. To that end, we performed intradermal injections of SLO in *Vav1cre-Lpcat3*$^{fl/fl}$ or *Lpcat3*$^{fl/fl}$ control mice. Skin was monitored up to 72 h after challenge for the appearance of ulceronecrotic lesions. *Vav1cre-Lpcat3*$^{fl/fl}$ mice developed larger lesions relative to *Lpcat3*$^{fl/fl}$ control mice **(Figure 4O, 4P).** Histological examination showed that *Vav1cre-Lpcat3*$^{fl/fl}$ mice displayed large areas of full-thickness skin and soft tissue necrosis, while *Lpcat3*-sufficient mice mostly displayed small areas of variable, partial-thickness necrosis **(Fig 4Q, 4R),** similar to chow-fed B6 mice. Similarly, we performed intradermal injections of SLO in *Cre/ERT2-Lpcat3*$^{fl/fl}$ (specific for endothelial cells) or *Lpcat3*$^{fl/fl}$ control mice. However, we didn't quite observe significantly greater lesion in the LPCAT3-deficient mice in endothelial cells, suggesting that specificity of CDCs could be more limited to certain cell types.

Loss of LPCAT3 increases skin and soft tissue necrosis in group A Strep infections

Finally, we asked if LPCAT3 deficiency in vascular endothelium and hematopoietic cells would influence the extent of tissue destruction observed from infection with invasive GAS (*S. pyogenes* stain 854 as above in Fig. 1). Remarkably, we observed that intradermal injection of GAS resulted in markedly larger skin ulcers in *Vav1cre-Lpcat3*$^{fl/fl}$ mice 48-72 h after injection **(Fig. 4S, 4T).** Gene expression data studies on infected lesions showed large increases in an array of inflammatory genes, including *Il1*b, *Tnfa*, *Cxcl1*, and interferon stimulated genes (*Ifnb*,

Mx1) relative to *Lpcat3*$^{fl/fl}$ control mice **(Fig. 4U).** Histopathologic evaluation revealed *Lpcat3*$^{fl/fl}$ control mice had ulceronecrotic lesions of the epidermis and dermis with early signs of abscess formation in the deep dermis and panniculus, with some spreading of edema, inflammatory cells, and bacteria along the fascial plane **(Fig. 4V).** In striking contrast, *Vav1cre-Lpcat3*$^{fl/f}$ transgenic mice demonstrated massive, full-thickness necrosis over large areas of tissue without signs of early abscess formation and spread of edema, inflammatory cells, and extension of the bacteria into the surrounding tissue **(Fig. 4V).** Together, these data show that tissue LPC homeostasis is an unappreciated but critical host metabolic factor that regulates the pathogenesis of necrotizing soft tissue infections by group A *strep*.

Methods

***Mouse strains**:* All WT mice were purchased from The Jackson Laboratory: WT C57BL/6 (JAX 000664). Lys2-cre (JAX 004781) & Vav1-iCre (JAX 008610) Lpcat3 (*LPCAT$^{fl/fl}$*) were kind gifts from Dr. Peter Tontonoz (UCLA).

***Cells**:* Bone marrow was differentiated into macrophages in DMEM containing 10% v/v FBS (HyClone, GE SH3007103), 5% v/v M-CSF conditioned media, 1% v/v pen/strep, 1% v/v glutamine (Invitrogen) 0.5% v/v sodium pyruvate (Invitrogen) for 7-9 days prior to experimental use. Cells were changed to media with 5% FBS at the time of stimulation. Mouse neutrophils were isolated from bone marrow and purified using EasySep^{TM} Mouse Neutrophil Enrichment Kit (StemCell) and were cultured in RPMI-1640 medium supplemented with 1% v/v pen/strep for up to 6 h.

Lipidomics Analysis: Macrophages were cultured in 6 well dishes (Fisher, 08-772-1B) and stimulated with DMSO, GW3965, or rosiglitazone. 48 h post-stimulation, cells were imaged for cell count as previously described, scraped and spun down in PBS, and snap-frozen as cell pellets. A modified Bligh and Dyer extraction was carried out on samples. Prior to biphasic extraction, a 13-lipid class Lipidyzer Internal Standard Mix is added to each sample (AB Sciex, 5040156). Following two successive extractions, pooled organic layers were dried down in a Genevac EZ-2 Elite. Lipid samples were resuspended in 1:1 methanol/dichloromethane with 10 mM Ammonium Acetate and transferred to robovials (ThermoFisher, 10800107) for analysis. Samples were analyzed on the Sciex Lipidyzer Platform for targeted quantitative measurement of 1100 lipid species across 13 classes. Differential Mobility Device on Lipidyzer was tuned with SelexION tuning kit (Sciex, 5040141). Instrument settings, tuning settings, and MRM list available upon request. Data analysis was performed according to the workflow published by Su, B. et al

***Isotope Enrichment Experiments*:** All isotope labeling experiments from BMDMs were performed as previously described. In brief, day 8 differentiated BMDMs were transferred to complete media containing 50% [13C]-glucose (Cambridge Isotope Laboratories, CLM-1396-MPT-PK) with DMSO or GW3965 for 48 h before collection. Analysis of labeled fatty acids and cholesterol was performed as described previously. The relative contributions of synthesis to the total cholesterol pool over the 48 h-labeling period were determined by fitting the isotopologue distributions for cholesterol in a model similar to Isotopomer Spectral Analysis (ISA) as described previously.

Preparation of S. pyogenes culture: *S. pyogenes* strain: GAS 854 was provided by Dr. Michael Wessels (Boston Children's Hospital). GAS was grown overnight in THY broth at 37°C Celsius, 5% CO_2 incubator. In the morning, a subculture (O.D. of 0.1) in THY broth was started and grown for 4hrs until the O.D. reaches between 0.65 – 0.7 (Approximately 2 x 10^8 cfu/mL). Bacteria was spun down at 800 g for 15 mins, washed once with PBS, and resuspended in 1 mL PBS (Approximately 5 x 10^6 CFU in 50 μL). Titers were confirmed by plating serial dilutions on blood agar plates.

***In vivo S. pyogenes infection*:** Experimental mice fedwere shaved on the lower back and were intradermally injected with 5 x 10^6 cfu *S. pyogenes.* 96 h later, photographs of the skin wounds were taken and lesion area (cm^2) was measured using the ImageJ software. Wounds were excised for histological analysis and bacteria burden studies.

***In vivo SLO injection*:** All *in vivo* SLO injections were performed as previously described (*23*). Mice fed on chow, high-fat (HF), and WD were shaved on the lower back and were intradermally injected with either PBS or SLO (8 kU/mouse). SLO was activated with 10 mM DTT at room temperature. 72 h later, photographs of the skin lesions were taken, and the lesion area (in cm^2) was measured using the ImageJ software. Subsequently, wild type C57/BL6 mice fed on either

chow or WD were shaved on the lower back and were either topically pre-treated with LXR agonist, GW3965 (10 mg/kg of mouse) for 24 h, or topically treated post-SLO injection (8 kU/mouse) at different time points. Lesion sizes were quantified as above 72 hours after injection. Finally, littermate matched wild type and Vav1-cre Lpcat3$^{fl/fl}$ mice driven were shaved on the lower back and were intradermally injected with SLO (8 ku/mouse). Lesion sizes were quantified as above 72 h after injection. Tissue samples were collected for histological analysis in UCLA Translational and Pathology Core Laboratory, as well as for RNA preparation in RNAlater™ Stabilizing Solution (ThermoFischer, Catalog No. AM7020).

RNA Extraction from skin tissues: Tissues were minced into smaller pieces in homogenizer tubes containing ceramic beads (Omni, SKU 19-646). 1 mL of Trizol (ThermoFisher, 15596-018) was added to each sample, and the tissues were homogenized using Omni Tissue Homogenizer (Omni, SKU 19-042E) at 3 cycles of 0.23 meters per second. The homogenized tubes were spun down for 10 minutes and the Trizol supernatant was transferred to another 1.5 mL tube for subsequent RNA extraction procedures using manufacturer's protocol.

Gene expression analysis: RNA was extracted from all cells with Trizol (ThermoFisher, 15596-018) using manufacturer's protocols. cDNA was synthesized with high-capacity cDNA reverse transcription kit (Applied Biosystems, 4368814) as per manufacturer's instructions (700 ng/μL RNA per cDNA synthesis reaction). Quantitative PCR (qPCR) was conducted on the Roche LightCycler 480 using SYBR Green Master Mix (Kapa Biosciences) or PowerUp™ SYBR™ Green Master Mix (ThermoFisher, A25778) and 0.5 μmol/L primers. Relative expression values are normalized to control gene (*36b4*) and expressed in terms of linear relative mRNA values. A list of qPCR primers are available upon request.

CDC Permeabilization Live Imaging: All *in vitro* CDC cytotoxicity assay were performed as previously described. BMDMs, neutrophils, HUVECs, and dermal fibroblasts were seeded 50

k/well on 96 well plates (E&K Scientific, EK-25090, Greiner). Cells were left for 2 days before stimulation with GW3965 or rosiglitazone for 24 h. Culture media were replaced by 37 ˚C PBS with 0.05% BSA, 1 μg/mL propidium iodide (PI) (VWR, 80057-368) and 5 μg/mL Hoechst 33342 (ThermoFisher, H3570). Then cells were challenged by spiking recombinant PFO (final concentration 1 nM) or gamma-irradiated SLO (final concentration 22 nM), and plates were imaged every 7 min on Molecular Devices ImageXpress XL using a 20x Objective (Nikon Plan Fluor, 0.3 NA). SLO was activated with the addition of 10 mM DTT in room temperature for 15 minutes. Total (Hoechst 33342-positive) and permeabilized (PI-positive) cell number were assessed using MetaXpress Software with Powercore using the Multi-wavelength cell scoring module.

Purification of ALO-D4, Conjugation of Fluorophore onto ALO-D4, and Binding of ALO-D4 onto Cells: These studies were performed as described previously. Briefly, ALO-D4 protein was purified using standard histidine-tagged affinity chromatography and concentrated into 1 mg/mL. Purified protein was conjugated with Alexa-594 and stored at 4˚C. Cells were seeded 100k/well and stimulated with DMSO, GW3965, or rosiglitazone for 24h. After stimulation, cells were incubated with ALO-D4, as described previously. Unbound proteins were removed by washing with PBS/Ca^{2+}/Mg^{2+} three times for 2 min each.

Quantification of Fluorescence Intensity: Fluorescent images were taken at UCLA Molecular Screening Shared Resource core facility on a Molecular Device ImageXpress Confocal using a 20x Objective (Nikon Plan Fluor, 0.3 NA). on a Molecular Devices ImageXpress XL. Maximum projected cellular fluorescence intensity was assessed by MetaXpress Software with Powercore using the Multi-wavelength cell scoring module, as described previously.

Histology: Skin was fixed overnight in 10% neutral buffered formalin followed by standard histologic processing. H&E stained slides were evaluated by a board certified

dermatopathologist. Histologic ulceration scores were determined according to the following scale: 0 – no ulceration/ erosion (only dermal inflammation and edema, 1- erosion, 2- erosion/ulceration, 3- epidermal ulceration, 4 – epidermal and dermal ulceration, 5 – full thickness ulceration of epidermis, dermis, and panniculus.

Figure Legends

Fig. 4 || (A, B) Quantification (nmol/10^7 cells) of lysoPC (16:0 and 18:0) and PC (16:0_18:2 and 16:0_20:4) species in WT or LPCAT3 KO BMDMs. **(C)** Expression of cholesterol metabolism genes from WT or *LysM-Cre LPCAT3$^{fl/fl}$* (designated LPCAT3 KO) BMDMs. **(D)** Net synthesized and total cholesterol (nmol/10^7 cells) from WT or LPCAT KO BMDMs. Total and synthesized cholesterol was measured by GC-MS using ISA modeling. **(E, F)** Percent PI+ from WT or *LPCAT3$^{fl/fl}$ LysM-cre* BMDMs upon challenge with perfringolysin O (PFO) for 60 mins or streptolysin O (SLO) for 4 h in media containing PI. Cells were imaged every 7 minutes to assess changes in PI influx. **(G)** Confocal images of WT or LPCAT KO BMDMs stained with fluorescent ALO-D4 and DAPI. Violin plots of cellular fluorescent intensity (n = 9,531, 10,384 cells measured). **(H)** Confocal images of WT or *LPCAT3$^{fl/fl}$ LysM-cre* BMDMs that were treated with Sphingomyelinase (SMase; 200 mU/mL) for 30 min at 37˚C, and then stained with fluorescent ALO-D4 and DAPI. Violin plots of cellular fluorescent intensity (n = 12,431, 14,113, 10,535, and 12,052 cells measured). **(I, J)** Representative images and lesion area of WT and *Vav1-Cre LPCAT3$^{fl/fl}$* mice challenged with intradermal SLO for 72h. Lesions are marked with white arrow. **(K)** Representative photomicrographs of H&E stained wound sections of mice in Fig. 4E. Yellow dashed line=erosion, gray dashed line=ulceration. Scale=500μm. **(L)** Histologic scoring of mice in (Fig 4E, F) treated with intradermal SLO for 72 hours. (**M, N)** Representative images and lesion area of WT and *Vav1-Cre LPCAT3$^{fl/fl}$* mice challenged intradermally with *S. pyogenes* (strain 854, 5 x 10^6 CFU per mouse) for 96h. Lesions are marked with white arrow. **(O)** Expression of inflammatory genes in skin tissues of WT and *LPCAT3$^{fl/fl}$ Vav1-cre* mice that were intradermally injected with *S. pyogenes*. **(P)** Representative photomicrographs of H&E stained wound sections of mice in Fig. 4H. Gray dashed line=ulceration. Scale=1000μm

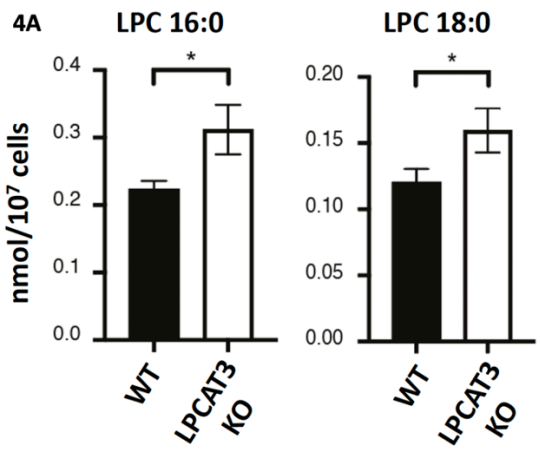
4A
LPC 16:0
LPC 18:0
nmol/10⁷ cells
WT
LPCAT3 KO

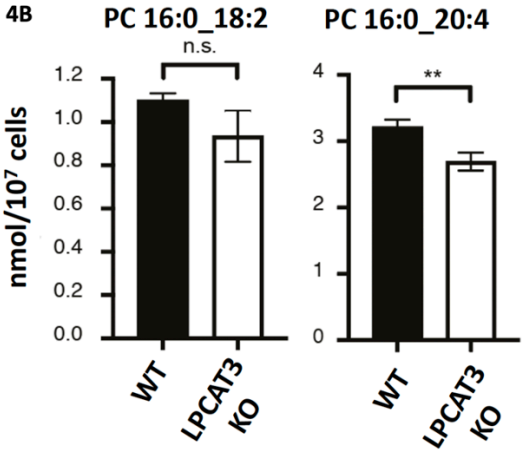
4B
PC 16:0_18:2
PC 16:0_20:4
n.s.
nmol/10⁷ cells
WT
LPCAT3 KO

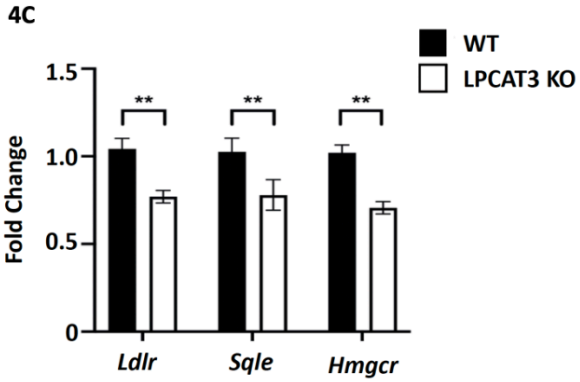
4C
WT
LPCAT3 KO
Fold Change
Ldlr
Sqle
Hmgcr

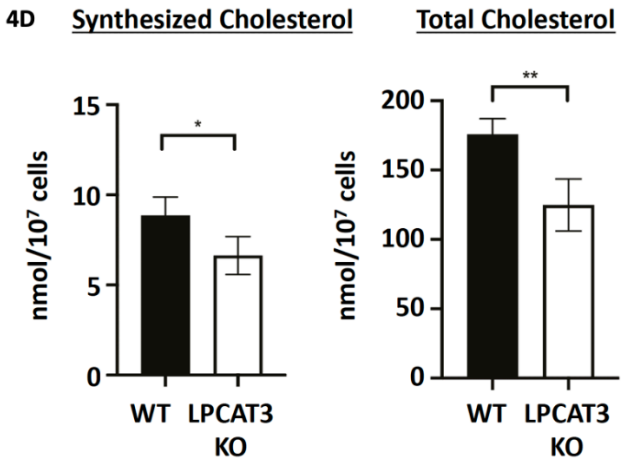
4D
Synthesized Cholesterol
Total Cholesterol
nmol/10⁷ cells
WT
LPCAT3 KO

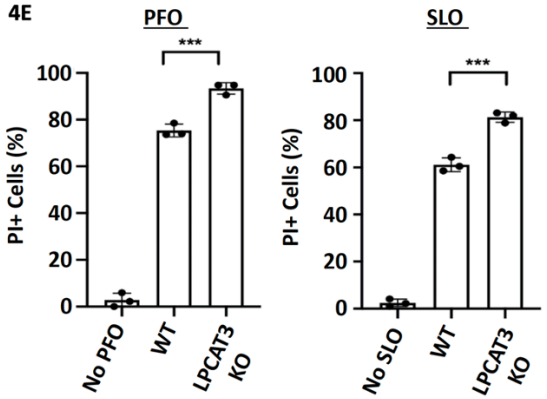
4E
PFO
SLO
PI+ Cells (%)
No PFO
WT
LPCAT3 KO
No SLO

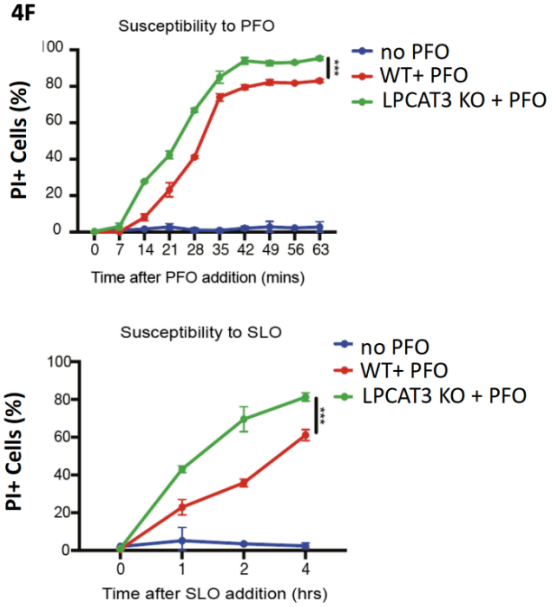
4F
Susceptibility to PFO
no PFO
WT+ PFO
LPCAT3 KO + PFO
PI+ Cells (%)
Time after PFO addition (mins)
Susceptibility to SLO
Time after SLO addition (hrs)

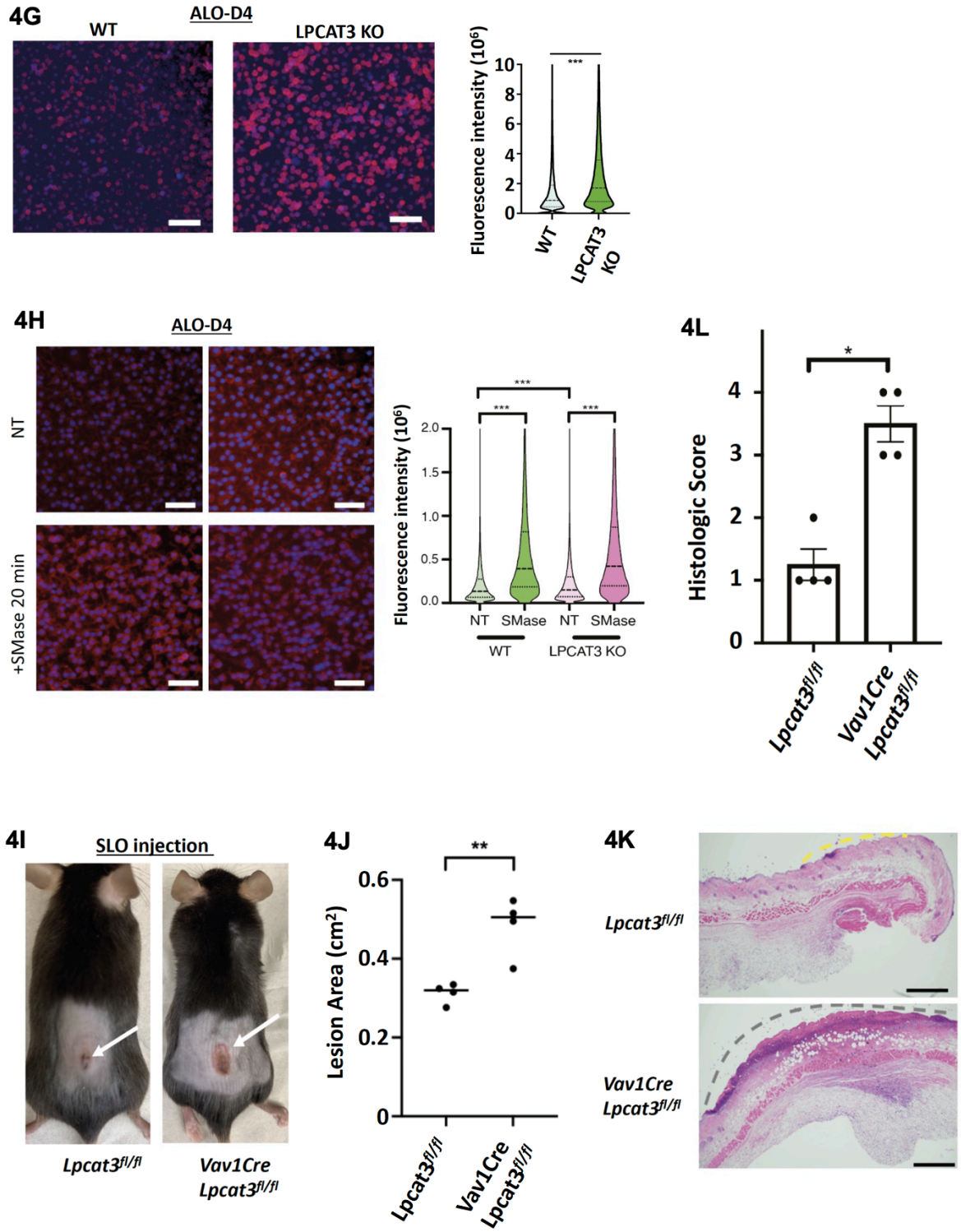
4G
ALO-D4
WT
LPCAT3 KO
Fluorescence intensity (10⁶)
***
WT
LPCAT3 KO
4H
ALO-D4
NT
+SMase 20 min
Fluorescence intensity (10⁶)
NT SMase NT SMase
WT
LPCAT3 KO
4L
Histologic Score
*
Lpcat3fl/fl
Vav1Cre Lpcat3fl/fl
4I
SLO injection
Lpcat3fl/fl
Vav1Cre Lpcat3fl/fl
4J
Lesion Area (cm²)
**
Lpcat3fl/fl
Vav1Cre Lpcat3fl/fl
4K
Lpcat3fl/fl
Vav1Cre Lpcat3fl/fl

4M

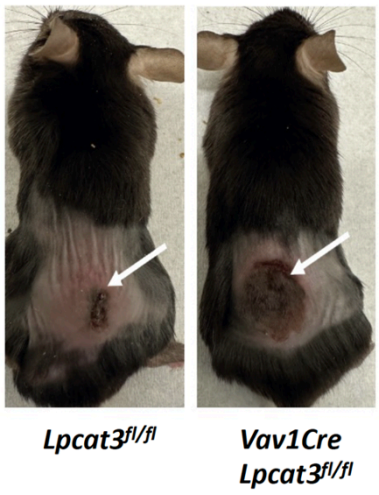
S. pyogenes infection
Lpcat3fl/fl
Vav1Cre
Lpcat3fl/fl

4N

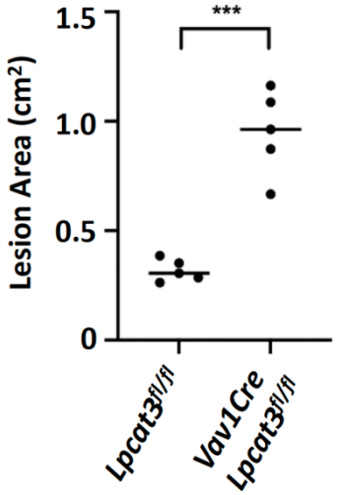
***
1.5
1.0
0.5
0
Lesion Area (cm2)
Lpcat3fl/fl
Vav1Cre
Lpcat3fl/fl

4O

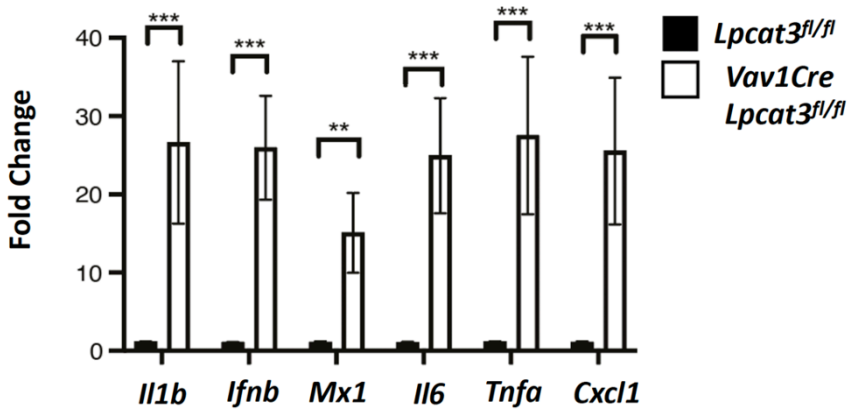
Fold Change
40
30
20
10
0
***
**
Il1b
Ifnb
Mx1
Il6
Tnfa
Cxcl1
Lpcat3fl/fl
Vav1Cre
Lpcat3fl/fl

4P

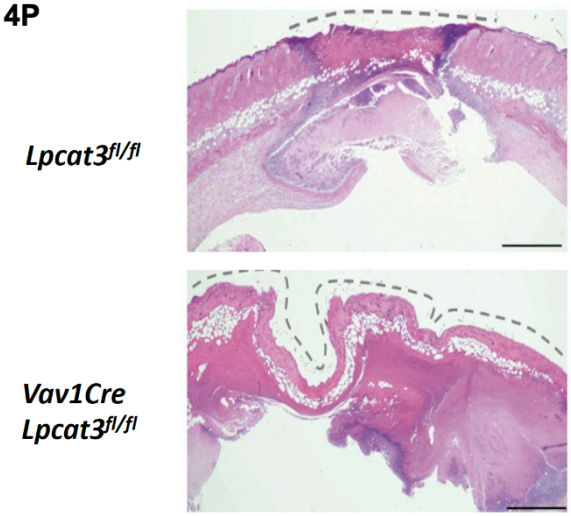
Lpcat3fl/fl
Vav1Cre
Lpcat3fl/fl

Chapter 5: Discussion and Future Directions

Discussion

Necrotizing soft tissue infections are medical and surgical emergencies resulting in substantial morbidity and mortality. As such, identifying host factors that underlie the pathogenesis of these challenging infections would undoubtedly be impactful. We first make a surprising discovery that a cholesterol-enriched Western diet influences the magnitude of tissue damage resulting from invasive GAS, but not high-fat diet enriched in saturated fatty acids. Remarkably, the increased tissue damage was dependent on the pore-forming toxin, SLO. Furthermore, our reductionist approach using SLO as a "proxy" of tissue infection recapitulated our findings in GAS infection studies. SLO is a cholesterol-dependent cytolysin that bind to a small pool of "accessible" cholesterol in the plasma membrane of host target cells, and we suspect that Western-diet expand the size of this critical pool the plasma membrane of cells such that CDCs emerge as a determinant of tissue damage. To our knowledge, this is the first example of a specific diet-toxin interaction modulating the pathogenesis of necrotizing soft tissue infections and highlights the complexity of host-microbe interactions. However, we cannot rule out the involvement of other virulence factors in mediating tissue destruction, such as Streptolysin S, another potent hemolysin, and a pore-forming toxin. It would be interesting to investigate the dependence of SLS by utilizing a SLS-deficient GAS infection model.

A logical supposition of our Western-diet GAS infection studies is that reducing the pool size of "accessible" cholesterol in infected and adjacent uninvolved tissues could be a means to reduce CDC-mediated tissue damage. Our previous manuscript in *Nature Immunology* started to investigate this concept of "accessible cholesterol pool" and cellular and tissue damage (*23*). As described in Chapter 2, we delineated a mechanism by which interferon signaling lowers the abundance of the accessible cholesterol via CH25H-dependent downregulation of *de novo* cholesterol synthesis. Likewise, CH25H-deficient macrophages and neutrophils show increases susceptibility to CDC-induced cytotoxicity as well as increased binding of the ALO-D4, which

was also recapitulated *in vivo.* Furthermore, cholesterol esterification is also required for maximal protection, which is supported by the data that inhibition of ACAT increases susceptibility to CDC-induced cytotoxicity. Finally, inhibition of cholesterol import and export cholesterol regulatory programs show altered response to CDCs—decreased susceptibility and increased susceptibility, respectively. It will be interesting to discover if other types of cytokine signaling would alter cell's sensitivity to CDCs. For instance, IL-1β is a pro-inflammatory cytokine that utilizes the MyD88 adaptor protein, just like TLR2. While we didn't rigorously test IL-1β signaling in the context of this study, we suspect that we will see a response that mirrors our findings that TLR2 signaling increases CDC susceptibility.

We find that pharmacologic activation of LXRs can induce protection from CDCs. This protection was dependent on the LXR receptors, but independent of interferon signaling. We also show that pharmacologic activation of LXR with a topical agonist can substantially reduced the magnitude of tissue damage resulting from intradermal injection of CDCs. Unlike interferon signaling however, LXR signaling doesn't alter *de novo* cholesterol biosynthesis, total cholesterol levels, cholesterol esterification, nor cholesterol efflux. Rather, we discovered that LXR signaling reduce the ability of CDC toxins to bind to target cells and induce cytotoxicity by reshaping lysophosphatidylcholine composition of target cells. These exciting results serve as a proof-of-concept that acute and local reprogramming of lipid metabolism in host tissues could be therapeutic strategy to induce resistive state to microbial toxins that target host lipids for their deleterious functions. Importantly, we showed that this tissue protection could be rapidly induced despite long-term Western-diet feeding. Thus, local pharmacologic reshaping of lipid composition in involved tissues could occur without having to correct systemic metabolic dysfunction of the individual. We imagine that induction of toxin resistant states could be employed to create limiting barrier that protect hosts from further tissue necrosis and bacterial

spreading, thereby halting disease progression. Additionally, preserving tissue architecture would undoubtedly enhance innate immune cell recruitment and function in infected tissues, ensure proper tissue oxygenation and metabolism, and enable better antibiotic perfusion.

The surprising discovery that cellular lysophosphatidylcholine (LPC) homeostasis regulates the pathogenesis of GAS infection or SLO toxin-mediated tissue necrosis has uncovered a link between phospholipid metabolism and the accessible cholesterol pool. The molecular mechanism by which increasing the LPCs pool results in heightened sensitivity to CDC-mediated tissue damage and susceptibility to GAS infection is likely multifactorial. However, our mechanistic data clearly implicates the influence of LPCs on the homeostasis of the accessible cholesterol pool targeted by CDCs for the effector function. As discussed in Chapter 2, the accessible pool is in rapid equilibrium with the ER cholesterol pool that regulates SREBP2 activity and cholesterol biosynthesis. Thus, expansion or contraction of the accessible cholesterol pool will result in decreased or increased cholesterol biosynthesis, respectively. This is in sharp contrast with our previous finding, in which we show that TRIF-dependent PRRs and interferon signaling reduces cholesterol biosynthesis, which is directly correlated with resistance to CDC cytotoxicity. However, our metabolism studies show that accumulation of LPC correlates with a marked reduction in expression of SREBP2 target genes, and correspondingly, decrease in *de novo* cholesterol biosynthesis, and total cellular cholesterol levels. Thus, cells with higher levels of LPCs behave metabolically as if they have excess cellular cholesterol accumulation despite lowered amounts of cholesterol. Previous work has shown that the accumulation of LPCs in the in membranes can disrupt cholesterol packing in microdomains in the plasma membrane via a detergent effect (*33*). In this system, liberated cholesterol would then flow into the accessible cholesterol pool resulting in increased CDC recognition, cytotoxicity and ultimately tissue damage. It may also be that LPCs shift accessible homeostasis through other

mechanisms. LPC are the precursor to such signaling through GPCRs or other bioactive lipid signaling pathways (*80, 81*).

In conclusion, my thesis work indicates that the lipid metabolic state of cells increases susceptibility to CDC-mediated cytotoxicity. My studies all show that diet and lipid composition of a host influences the magnitude of tissue destruction in GAS infection. These results advance our understanding of the pathogenesis of necrotizing infections, and suggest that pharmacologic reprogramming of lipid metabolism in infected, and adjacent tissues, could be used to minimize tissue damage. We expect that this strategy would also increase deliverer of antibiotics by preserving vasculature architecture and bolster innate immunity. We expect these observations to open many new avenues of investigation and are excited to determine if these concepts can be translated into new treatment strategies to limit the extreme morbidity and mortality for NF and related necrotizing soft tissue infections.

References

1. R. Puvanendran, J. C. Huey, S. Pasupathy, Necrotizing fasciitis. *Can Fam Physician* **55**, 981-987 (2009).
2. A. A. Hysong *et al.*, Necrotizing Fasciitis: Pillaging the Acute Phase Response. *J Bone Joint Surg Am* **102**, 526-537 (2020).
3. E. Tunovic *et al.*, Necrotizing fasciitis: a six-year experience. *J Burn Care Res* **33**, 93-100 (2012).
4. L. L. Chen, B. Fasolka, C. Treacy, Necrotizing fasciitis: A comprehensive review. *Nursing* **50**, 34-40 (2020).
5. P. Tantirat, T. Rattanathumsakul, H. Praekunatham, K. Pachanee, R. Suphanchaimat, Epidemiological Situation of Necrotizing Fasciitis and Factors in Thailand and Factors Associated with Its Morbidity and Mortality, 2014-2018. *Risk Manag Healthc Policy* **13**, 1613-1624 (2020).
6. D. L. Stevens, A. E. Bryant, Necrotizing Soft-Tissue Infections. *N Engl J Med* **377**, 2253-2265 (2017).
7. Z. Al-Qurayshi, R. L. Nichols, M. T. Killackey, E. Kandil, Mortality Risk in Necrotizing Fasciitis: National Prevalence, Trend, and Burden. *Surg Infect (Larchmt)* **21**, 840-852 (2020).
8. C. J. Andersen, K. E. Murphy, M. L. Fernandez, Impact of Obesity and Metabolic Syndrome on Immunity. *Adv Nutr* **7**, 66-75 (2016).
9. T. Bruun *et al.*, Necrotizing soft tissue infections caused by Streptococcus pyogenes and Streptococcus dysgalactiae subsp. equisimilis of groups C and G in western Norway. *Clin Microbiol Infect* **19**, E545-550 (2013).
10. D. K. Das, M. G. Baker, K. Venugopal, Risk factors, microbiological findings and outcomes of necrotizing fasciitis in New Zealand: a retrospective chart review. *BMC Infect Dis* **12**, 348 (2012).

11. L. J. Zhang *et al.*, Diet-induced obesity promotes infection by impairment of the innate antimicrobial defense function of dermal adipocyte progenitors. *Sci Transl Med* **13**, (2021).
12. N. J. Avire, H. Whiley, K. Ross, A Review of Streptococcus pyogenes: Public Health Risk Factors, Prevention and Control. *Pathogens* **10**, (2021).
13. C. D. Ashbaugh, H. B. Warren, V. J. Carey, M. R. Wessels, Molecular analysis of the role of the group A streptococcal cysteine protease, hyaluronic acid capsule, and M protein in a murine model of human invasive soft-tissue infection. *J Clin Invest* **102**, 550-560 (1998).
14. B. T. Russo *et al.*, The M Protein of Streptococcus pyogenes Strain AP53 Retains Cell Surface Functional Plasminogen Binding after Inactivation of the Sortase A Gene. *J Bacteriol* **202**, (2020).
15. H. Sjölinder *et al.*, The ScpC protease of Streptococcus pyogenes affects the outcome of sepsis in a murine model. *Infect Immun* **76**, 3959-3966 (2008).
16. D. E. Hammers *et al.*, Streptolysin S targets the sodium-bicarbonate cotransporter NBCn1 to induce inflammation and cytotoxicity in human keratinocytes during Group A Streptococcal infection. *Front Cell Infect Microbiol* **12**, 1002230 (2022).
17. P. Bhattacharjee, P. A. Keyel, Cholesterol-dependent cytolysins impair pro-inflammatory macrophage responses. *Scientific Reports* **8**, 6458 (2018).
18. I. Gryllos *et al.*, PerR confers phagocytic killing resistance and allows pharyngeal colonization by group A Streptococcus. *PLoS Pathog* **4**, e1000145 (2008).
19. I. Gryllos *et al.*, Induction of group A Streptococcus virulence by a human antimicrobial peptide. *Proc Natl Acad Sci U S A* **105**, 16755-16760 (2008).
20. J. Clarke *et al.*, Streptolysin O concentration and activity is central to in vivo phenotype and disease outcome in Group A Streptococcus infection. *Sci Rep* **11**, 19011 (2021).

21. G. Sierig, C. Cywes, M. R. Wessels, C. D. Ashbaugh, Cytotoxic effects of streptolysin o and streptolysin s enhance the virulence of poorly encapsulated group a streptococci. *Infect Immun* **71**, 446-455 (2003).

22. F. A. Pinho-Ribeiro *et al.*, Blocking Neuronal Signaling to Immune Cells Treats Streptococcal Invasive Infection. *Cell* **173**, 1083-1097.e1022 (2018).

23. Q. D. Zhou *et al.*, Interferon-mediated reprogramming of membrane cholesterol to evade bacterial toxins. *Nat Immunol* **21**, 746-755 (2020).

24. R. Thapa, S. Ray, P. A. Keyel, Interaction of Macrophages and Cholesterol-Dependent Cytolysins: The Impact on Immune Response and Cellular Survival. *Toxins (Basel)* **12**, (2020).

25. A. T. Nishimoto, J. W. Rosch, E. I. Tuomanen, Pneumolysin: Pathogenesis and Therapeutic Target. *Front Microbiol* **11**, 1543 (2020).

26. Z. Wang, X. Tao, S. Liu, Y. Zhao, X. Yang, An Update Review on Listeria Infection in Pregnancy. *Infect Drug Resist* **14**, 1967-1978 (2021).

27. R. K. Tweten, Cholesterol-dependent cytolysins, a family of versatile pore-forming toxins. *Infect Immun* **73**, 6199-6209 (2005).

28. A. Gay, D. Rye, A. Radhakrishnan, Switch-like responses of two cholesterol sensors do not require protein oligomerization in membranes. *Biophys J* **108**, 1459-1469 (2015).

29. D. Z. de Back, E. B. Kostova, M. van Kraaij, T. K. van den Berg, R. van Bruggen, Of macrophages and red blood cells; a complex love story. *Front Physiol* **5**, 9 (2014).

30. S. T. Cooper, P. L. McNeil, Membrane Repair: Mechanisms and Pathophysiology. *Physiol Rev* **95**, 1205-1240 (2015).

31. J. W. Clancy, M. Schmidtmann, C. D'Souza-Schorey, The ins and outs of microvesicles. *FASEB Bioadv* **3**, 399-406 (2021).

32. A. Read, M. Schröder, The Unfolded Protein Response: An Overview. *Biology (Basel)* **10**, (2021).

33. A. Das, M. S. Brown, D. D. Anderson, J. L. Goldstein, A. Radhakrishnan, Three pools of plasma membrane cholesterol and their relation to cholesterol homeostasis. *Elife* **3**, (2014).

34. M. S. Lee, S. J. Bensinger, Reprogramming cholesterol metabolism in macrophages and its role in host defense against cholesterol-dependent cytolysins. *Cell Mol Immunol* **19**, 327-336 (2022).

35. K. A. Johnson, S. Endapally, D. C. Vazquez, R. E. Infante, A. Radhakrishnan, Ostreolysin A and anthrolysin O use different mechanisms to control movement of cholesterol from the plasma membrane to the endoplasmic reticulum. *J Biol Chem* **294**, 17289-17300 (2019).

36. D. K. O'Brien, S. B. Melville, Effects of Clostridium perfringens alpha-toxin (PLC) and perfringolysin O (PFO) on cytotoxicity to macrophages, on escape from the phagosomes of macrophages, and on persistence of C. perfringens in host tissues. *Infect Immun* **72**, 5204-5215 (2004).

37. J. Luo, H. Yang, B. L. Song, Mechanisms and regulation of cholesterol homeostasis. *Nat Rev Mol Cell Biol* **21**, 225-245 (2020).

38. M. S. Brown, A. Radhakrishnan, J. L. Goldstein, Retrospective on Cholesterol Homeostasis: The Central Role of Scap. *Annu Rev Biochem* **87**, 783-807 (2018).

39. A. J. Brown, L. Sun, J. D. Feramisco, M. S. Brown, J. L. Goldstein, Cholesterol addition to ER membranes alters conformation of SCAP, the SREBP escort protein that regulates cholesterol metabolism. *Mol Cell* **10**, 237-245 (2002).

40. S. Y. Liu *et al.*, Interferon-inducible cholesterol-25-hydroxylase broadly inhibits viral entry by production of 25-hydroxycholesterol. *Immunity* **38**, 92-105 (2013).

41. G. W. Go, A. Mani, Low-density lipoprotein receptor (LDLR) family orchestrates cholesterol homeostasis. *Yale J Biol Med* **85**, 19-28 (2012).

42. M. M. Beyea *et al.*, Selective up-regulation of LXR-regulated genes ABCA1, ABCG1, and APOE in macrophages through increased endogenous synthesis of 24(S),25-epoxycholesterol. *J Biol Chem* **282**, 5207-5216 (2007).

43. A. Ouvrier *et al.*, LXR and ABCA1 control cholesterol homeostasis in the proximal mouse epididymis in a cell-specific manner. *J Lipid Res* **50**, 1766-1775 (2009).

44. T. Y. Chang *et al.*, Roles of acyl-coenzyme A:cholesterol acyltransferase-1 and -2. *Curr Opin Lipidol* **12**, 289-296 (2001).

45. S. Raychaudhuri, W. A. Prinz, The diverse functions of oxysterol-binding proteins. *Annu Rev Cell Dev Biol* **26**, 157-177 (2010).

46. J. Sandhu *et al.*, Aster Proteins Facilitate Nonvesicular Plasma Membrane to ER Cholesterol Transport in Mammalian Cells. *Cell* **175**, 514-529.e520 (2018).

47. A. Ferrari *et al.*, Aster Proteins Regulate the Accessible Cholesterol Pool in the Plasma Membrane. *Mol Cell Biol* **40**, (2020).

48. S. Endapally, R. E. Infante, A. Radhakrishnan, Monitoring and Modulating Intracellular Cholesterol Trafficking Using ALOD4, a Cholesterol-Binding Protein. *Methods Mol Biol* **1949**, 153-163 (2019).

49. W. Y. Hsieh *et al.*, Toll-Like Receptors Induce Signal-Specific Reprogramming of the Macrophage Lipidome. *Cell Metab* **32**, 128-143.e125 (2020).

50. W. Huang, C. K. Glass, Nuclear receptors and inflammation control: molecular mechanisms and pathophysiological relevance. *Arterioscler Thromb Vasc Biol* **30**, 1542-1549 (2010).

51. K. Wang, Y. J. Wan, Nuclear receptors and inflammatory diseases. *Exp Biol Med (Maywood)* **233**, 496-506 (2008).

52. N. Zelcer, C. Hong, R. Boyadjian, P. Tontonoz, LXR regulates cholesterol uptake through Idol-dependent ubiquitination of the LDL receptor. *Science* **325**, 100-104 (2009).

53. B. Wang, P. Tontonoz, Liver X receptors in lipid signalling and membrane homeostasis. *Nat Rev Endocrinol* **14**, 452-463 (2018).

54. K. Chu, M. Miyazaki, W. C. Man, J. M. Ntambi, Stearoyl-coenzyme A desaturase 1 deficiency protects against hypertriglyceridemia and increases plasma high-density lipoprotein cholesterol induced by liver X receptor activation. *Mol Cell Biol* **26**, 6786-6798 (2006).

55. X. Rong *et al.*, LXRs regulate ER stress and inflammation through dynamic modulation of membrane phospholipid composition. *Cell Metab* **18**, 685-697 (2013).

56. D. G. Thomas *et al.*, LXR Suppresses Inflammatory Gene Expression and Neutrophil Migration through cis-Repression and Cholesterol Efflux. *Cell Rep* **25**, 3774-3785.e3774 (2018).

57. A. Ito *et al.*, LXRs link metabolism to inflammation through Abca1-dependent regulation of membrane composition and TLR signaling. *Elife* **4**, e08009 (2015).

58. M. Ahmadian *et al.*, PPARγ signaling and metabolism: the good, the bad and the future. *Nat Med* **19**, 557-566 (2013).

59. S. Tyagi, P. Gupta, A. S. Saini, C. Kaushal, S. Sharma, The peroxisome proliferator-activated receptor: A family of nuclear receptors role in various diseases. *J Adv Pharm Technol Res* **2**, 236-240 (2011).

60. J. Youssef, M. Badr, Role of Peroxisome Proliferator-Activated Receptors in Inflammation Control. *J Biomed Biotechnol* **2004**, 156-166 (2004).

61. X. Hu *et al.*, Release of cholesterol-rich particles from the macrophage plasma membrane during movement of filopodia and lamellipodia. *Elife* **8**, (2019).

62. M. Ishibashi *et al.*, Liver x receptor regulates arachidonic acid distribution and eicosanoid release in human macrophages: a key role for lysophosphatidylcholine acyltransferase 3. *Arterioscler Thromb Vasc Biol* **33**, 1171-1179 (2013).

63. N. S. Chandel, Lipid Metabolism. *Cold Spring Harb Perspect Biol* **13**, (2021).

64. D. Gompertz, Phospholipids and their metabolism. *J Clin Pathol Suppl (Assoc Clin Pathol)* **5**, 11-16 (1973).

65. V. A. Fadok, D. L. Bratton, S. C. Frasch, M. L. Warner, P. M. Henson, The role of phosphatidylserine in recognition of apoptotic cells by phagocytes. *Cell Death Differ* **5**, 551-562 (1998).

66. X. Wang, L. B. Hills, Y. H. Huang, Lipid and Protein Co-Regulation of PI3K Effectors Akt and Itk in Lymphocytes. *Front Immunol* **6**, 117 (2015).

67. K. M. Siess, T. A. Leonard, Lipid-dependent Akt-ivity: where, when, and how. *Biochem Soc Trans* **47**, 897-908 (2019).

68. M. Z. Ashraf, N. S. Kar, E. A. Podrez, Oxidized phospholipids: biomarker for cardiovascular diseases. *Int J Biochem Cell Biol* **41**, 1241-1244 (2009).

69. B. Wang, P. Tontonoz, Phospholipid Remodeling in Physiology and Disease. *Annu Rev Physiol* **81**, 165-188 (2019).

70. J. N. van der Veen *et al.*, The critical role of phosphatidylcholine and phosphatidylethanolamine metabolism in health and disease. *Biochim Biophys Acta Biomembr* **1859**, 1558-1572 (2017).

71. R. Pichot, R. L. Watson, I. T. Norton, Phospholipids at the interface: current trends and challenges. *Int J Mol Sci* **14**, 11767-11794 (2013).

72. F. Gibellini, T. K. Smith, The Kennedy pathway--De novo synthesis of phosphatidylethanolamine and phosphatidylcholine. *IUBMB Life* **62**, 414-428 (2010).

73. C. R. McMaster, From yeast to humans - roles of the Kennedy pathway for phosphatidylcholine synthesis. *FEBS Lett* **592**, 1256-1272 (2018).

74. V. B. O'Donnell, New appreciation for an old pathway: the Lands Cycle moves into new arenas in health and disease. *Biochem Soc Trans* **50**, 1-11 (2022).

75. L. Wang *et al.*, Metabolic interactions between the Lands cycle and the Kennedy pathway of glycerolipid synthesis in Arabidopsis developing seeds. *Plant Cell* **24**, 4652-4669 (2012).

76. H. Shindou, T. Shimizu, Acyl-CoA:lysophospholipid acyltransferases. *J Biol Chem* **284**, 1-5 (2009).

77. S. Lin, M. Ikegami, C. Moon, A. P. Naren, J. M. Shannon, Lysophosphatidylcholine Acyltransferase 1 (LPCAT1) Specifically Interacts with Phospholipid Transfer Protein StarD10 to Facilitate Surfactant Phospholipid Trafficking in Alveolar Type II Cells. *J Biol Chem* **290**, 18559-18574 (2015).

78. W. Abate, H. Alrammah, M. Kiernan, A. J. Tonks, S. K. Jackson, Lysophosphatidylcholine acyltransferase 2 (LPCAT2) co-localises with TLR4 and regulates macrophage inflammatory gene expression in response to LPS. *Sci Rep* **10**, 10355 (2020).

79. X. Rong *et al.*, Lpcat3-dependent production of arachidonoyl phospholipids is a key determinant of triglyceride secretion. *Elife* **4**, (2015).

80. Y. F. Li *et al.*, Lysophospholipids and their G protein-coupled receptors in atherosclerosis. *Front Biosci (Landmark Ed)* **21**, 70-88 (2016).

81. L. Wang *et al.*, Lysophosphatidylcholine-induced surface redistribution regulates signaling of the murine G protein-coupled receptor G2A. *Mol Biol Cell* **16**, 2234-2247 (2005).